Generated using the official AMS LaTeX template v6.1

Disentangling mechanisms controlling atmospheric transport and mixing processes over mountain areas at different space- and time-scales: the field campaign of the project DECIPHER on Monte Baldo (Italian Alps)

Giorgio Doglioni,[a] Francesco Barbano[b,c] Elena Barbaro [d] Barbara Biasuzzi [e] Alessandro Bracci [f] Christophe Brun [g] Warren R.L. Cairns [d] Sebastiano Carpentari [a] Massimo Cassiani [a,h] Franz Conen [i] Giulio Cozzi [d] Gianmarco Cracco [e] Federico Dallo [d] Fabrizio De Blasi [d] Costanza Di Felice Fabrizi [b,j] Paolo Di Girolamo [k] Luca Di Liberto [f] Marco Di Paolantonio [l] Silvana Di Sabatino [c] Davide Dionisi [l] Annika Einbock [i] Théo Fernandez [g] Angelo Finco [m] Emmanuel Francisco-Alcantara [s] Enrico Gazzola [e] Giacomo Gerosa [m] Stefano Gianessi [e] Lorenzo Giovannini [a] Louis Gostiaux [v] Muriel Lagauzere [g] Riccardo Marzuoli [m] Christian Nardon [a] Ahmed Njimongbet [a] Ferdinando Pasqualini [f] Nathan Philippot [u] Davide Plebani [m,n] Davide Poggi [o] Federico Porcù [c] Akanksha Rajput [a] Florencia Rodriguez [s] Claudia Rossetti [d] Mira Shivani Sankar [b,p] Donato Summa [q] Nadia Vendrame [r] Dino Zardi [a,b]

[a] *Department of Civil, Environmental and Mechanical Engineering (DICAM), University of Trento, Trento, Italy.* [b] *Center Agriculture Food Environment (C3A), University of Trento, San Michele all'Adige, Italy.* [c] *Department of Physics and Astronomy "Augusto Righi", University of Bologna, Bologna, Italy.* [d] *Institute of Polar Sciences, National Research Council (CNR ISP), Venice, Italy.* [e] *FINAPP S.p.A., Via del Commercio 27, 35036 Padova (PD), Italy* [f] *Institute of Atmospheric Sciences and Climate, National Research Council (CNR ISAC), Italy.* [g] *Laboratoire des Écoulements Géophysiques et Industriels (LEGI), Université Grenoble Alpes, Grenoble, France.* [h] *Norwegian Institute for Air Research (NILU), Kjeller, Norway.* [i] *Department of Environmental Sciences, University of Basel, Basel, Switzerland.* [j] *National Doctoral School in Polar Sciences, University of Venice "Ca' Foscari", Venice, Italy.* [k] *Department of Health Sciences (DISS), University of Basilicata, Potenza, Italy.* [l] *Institute of Marine Sciences, National Research Council (CNR-ISMAR), Rome, Italy.* [m] *Faculty of Mathematical, Physical and Natural*

Sciences, Catholic University of the Sacred Heart, Brescia, Italy. [n] *Department of Earth and Environmental Sciences, KU Leuven, Belgium.* [o] *Department of Environment, Land and Infrastructure Engineering (DIATI), Politecnico di Torino, Torino, Italy.* [p] *University School for Advanced Studies (IUSS Pavia), Pavia, Italy.* [q] *Institute of Methodologies for Environmental Analysis, National Research Council (IMAA-CNR), Tito Scalo, Italy.* [r] *Research and Innovation Centre, Fondazione Edmund Mach (FEM), San Michele all'Adige, Italy.* [s] *Morphodynamique Continentale et Côtière (M2C), University of Rouen Normandy, Rouen, France.* [t] *Institut des Géosciences de l'Environnement (IGE), Université Grenoble Alpes, Grenoble, France.* [u] *CNRM, Météo-France, Toulouse, France.* [v] *CNRS, Ecole Centrale de Lyon, INSA Lyon, Université Lyon 1, LMFA, UMR5509, Ecully, France*

Corresponding author: Giorgio Doglioni, giorgio.doglioni@unitn.it

ABSTRACT: This paper presents the experimental campaign of the international project DECIPHER (Disentangling mechanisms controlling atmospheric transport and mixing processes over mountain areas at different space and timescales), which investigates atmospheric transport and exchange over mountains, with particular emphasis on daily-periodic, thermally driven slope winds. Turbulence in the mountainous boundary layer remains incompletely understood and inadequately represented in weather and climate models. DECIPHER addresses this gap by characterizing transport and exchange associated with slope winds and their dependence on ambient stability and surface forcing. The project is connected to TEAMx, an international program aimed at improving understanding and numerical representation of mountain-atmosphere processes. An intensive field campaign was conducted from mid-June to mid-October 2025 on a steep, east-facing slope of Monte Baldo (45°39'56.0"N, 10°49'10.9"E) in the Alps. A broad set of instruments was deployed to observe processes across scales. Multi-level flux systems on towers monitored turbulence at different elevations, while three wind lidars measured along- and cross-slope winds. Particulate matter, temperature, and humidity were continuously monitored along the slope. Vertical profiles of thermodynamic and compositional properties were obtained using a tethered balloon and a vertically pointing Raman lidar. Additional measurements included high-frequency near-surface turbulence profiling and distributed soil-moisture monitoring with a cosmic-ray neutron sensor. The four-month campaign captured a wide range of seasonal and weather conditions. Preliminary analyses reveal distinct patterns in local circulations and their links to turbulent structures and multi-scale atmospheric transport.

SIGNIFICANCE STATEMENT: Mountainous terrain significantly affects the overlying atmosphere. The diverse exposure of landforms to the incoming solar radiation leads to uneven heating, driving atmospheric circulations and transport processes across multiple scales. Understanding these processes is fundamental to meteorology, as the skill of weather forecasts in mountainous terrain depends on how accurately they are represented in numerical weather prediction models. Our work advances the understanding of atmospheric flows in mountainous terrain through high-quality observations specifically designed to capture slope-flow dynamics. During the DECIPHER observational campaign carried out on a regular slope of Monte Baldo in the southern Italian Alps, we identified and documented remarkable features of slope flows. This paper presents the campaign and showcases the ongoing studies enabled by the collected dataset.

CAPSULE: The observational campaign of the DECIPHER project produced a rich, diverse, and innovative dataset designed to study thermally driven slope winds and associated multiscale transport and exchange processes.

Mountainous terrain affects atmospheric motion on a wide range of spatial and temporal scales, from planetary waves and regional circulations to local slope flows and turbulence (Whiteman 2000). At regional to local scales, the uneven radiative heating and cooling of inhomogeneous and/or tilted surfaces generate thermally driven wind systems that transport and mix heat, momentum, moisture, and atmospheric constituents between the surface and the overlying atmosphere. Through their bidirectional interactions with convection and larger-scale forcing, these flows constitute a fundamental component of the mountain boundary layer (MoBL) (Lehner and Rotach 2018) and modulate transport and exchange processes in regions with rugged orography.

Thermally driven slope winds are a prime example of such wind systems. As inclined surfaces alternate heating and cooling over the diurnal cycle, along-slope buoyancy and pressure gradients generate upslope (anabatic) and downslope (katabatic) winds whenever local forcing is not overwhelmed by larger-scale winds (Zardi and Whiteman 2013). Although they develop locally, and typically evolve over time scales of minutes to hours, their influence extends beyond the immediate slope, becoming a multi-scale phenomenon: intrinsic near-surface characteristics, such as the jet-like shape of the profile, which increases turbulence intensity (Oldroyd et al. 2016), combine with advection (Farina and Zardi 2023), sub-mesoscale (Barbano et al. 2022) and convective (Cintolesi et al. 2021) flows, causing non-stationary motions and large-scale interactions. By coupling surface exchange and turbulence with valley circulations, boundary-layer development, ridge-level transport, and potentially the free atmosphere, they provide an important pathway through which locally generated motions affect transport and mixing over larger spatial and temporal scales (Leukauf et al. 2016). Being ubiquitous in mountain terrain, slope winds are among the building blocks of the mountain boundary layer circulation system (Fig. 1).

Despite their importance, thermally driven slope flows and their associated exchange processes remain difficult to observe, model, and ultimately to understand (Farina and Zardi 2023). Measurements in complex terrain are strongly influenced by local geometry, elevation, surface properties, and exposure, and therefore often have limited spatial representativeness (Emeis et al. 2018). Models face complementary challenges associated with finite resolution, unresolved terrain heterogeneity, approximate turbulence parameterizations (Chow et al. 2019), and limitations in data assimilation over complex topography (Hacker et al. 2018). Consequently, the mechanisms controlling slope-flow development, turbulent mixing and the associated tracer transport, mountain

venting, and convective development remain difficult to isolate and quantify. These limitations reduce our ability to provide reliable information for weather and air-quality forecasting (Giovannini et al. 2020), renewable-energy assessment, agrometeorology, hydrology, and resource management in mountainous regions and their surroundings (De Wekker et al. 2018).

Several field campaigns included observations of slope winds in mountainous terrain. Prominent examples are METCRAX-I and METCRAX-II (Whiteman et al. 2008; Lehner et al. 2016), MAP-Riviera (Rotach et al. 2004), and MATERHORN (Fernando et al. 2015): a comprehensive overview is provided by Farina and Zardi (2023). These campaigns produced valuable observations of mountain flows and turbulence, but the most associated studies focused on katabatic winds, with fewer addressing the anabatic counterpart. Moreover, none was designed specifically to investigate the coupled dynamics, turbulence, transport, and mixing associated with both up- and down-slope flows as a main goal.

To address this gap, an extended international consortium of partners joined an experimental initiative under the scheme of the project DECIPHER (Disentangling mechanisms controlling atmospheric transport and mixing processes over mountain areas at different space and timescales), funded by the European Union under the Next Generation EU PRIN 2022 funding scheme (more details on the project can be found on the website `https://sites.google.com/unitn.it/decipherproject/home-page`. Specifically, a coordinated field campaign was designed to combine fundamental observations of slope-flow dynamics and turbulence with measurements of particulate matter, ozone concentrations and thermodynamic properties in the lower troposphere. Thirteen universities and research centers deployed a multi-instrument observational setup on a steep, regular, and quite homogeneous east-facing slope of Monte Baldo (Fig. 1) in the Italian Alps from 10 June to 20 October 2025. The experiment combined near-surface and turbulence measurements, vertical profiling, remote sensing, and atmospheric-composition observations. This integrated strategy was designed not only to characterize anabatic and katabatic flows, but also to determine how thermally driven circulations transport, redistribute, and mix atmospheric constituents within the mountain boundary layer. The suitability of this site was determined in the preliminary field campaign of the DECIPHER project in 2024, described in Rajput et al. (2026).

Hence, DECIPHER sought to disentangle the chain of processes linking radiative surface forcing to slope-flow development, turbulence, transport, flow separation, and exchange with the wider

mountain atmosphere. In particular, the campaign aimed to distinguish the intrinsic response of thermally driven slope flows from their modulation by atmospheric stability, valley-scale circulations, surface heterogeneity, and larger-scale winds. It was also meant to separate organized along-slope advection from turbulent mixing, and local redistribution of particulate matter and ozone from effective exchange with the valley atmosphere and the free atmosphere.

Accordingly, the main processes targeted by DECIPHER were:

- *Turbulence and surface exchange.* Characterizing turbulence in anabatic and katabatic flows and its role in the exchange of momentum, heat, moisture, and atmospheric constituents (Serafin et al. 2018; Charrondière et al. 2022a).

- *Flow structure and idealized theory.* Assessing how observed flow depth, velocity, stratification, and turbulence compare with analytical models and idealized numerical simulations (Prandtl 1942; Defant 1949; Serafin and Zardi 2010; Zardi and Serafin 2015; Giometto et al. 2017; Brun et al. 2017).

- *Tracer transport, mixing, and mountain venting.* Quantifying the transport and redistribution of particulate matter, ozone, and air masses along the slope, and distinguishing organized advection from turbulent mixing and local recirculation from export out of the mountain boundary layer (De Wekker and Kossmann 2015; Pardyjak et al. 2009).

- *Flow separation and convection.* Investigating the detachment of katabatic and anabatic flows from the surface (Hocut et al. 2015), their contribution to vertical transport, and their possible role in the initiation of orographic convection (Kirshbaum et al. 2018; Banta et al. 2016; Demko and Geerts 2010; Geerts et al. 2008).

- *Morning and evening transitions.* Examining the timing and structure of the reversal from downslope to upslope flow and their dependence on surface forcing, ambient stability, background winds, and residual layers (Farina et al. 2023; Nadeau et al. 2013, 2020; Lehner et al. 2015).

- *Interactions across the mountain wind system.* Determining how slope winds interact with valley winds, convective circulations, and regional mountain–plain systems to control recirculation, mixing, entrainment, and export of heat and atmospheric constituents (Lehner et al. 2015; Brogno et al. 2021).

Altogether, these objectives provide a framework for relating surface forcing and slope-flow dynamics to turbulence and atmospheric-composition changes, and for assessing how processes initiated at the scale of an individual slope contribute to transport and exchange across the wider mountain atmosphere.

Conducted within the broader TEAMx framework, described in Box a, DECIPHER produced a dedicated dataset to evaluate idealized concepts of slope-flow dynamics, investigate thermally driven transport and mixing, and improve their representation in atmospheric models. The aim of this paper is to outline the scientific motivation, observational strategy, instrumentation, and meteorological context of the campaign, and to illustrate the dataset's potential through selected examples of the targeted processes. The article is organized as follows. Sections 1 and 2 describe the study area and observational strategy, respectively. Section 3 summarizes the meteorological conditions observed during the campaign and places them in the context of the local climatology. Selected preliminary results are presented in Section 4, followed by a discussion of the scientific perspectives enabled by the dataset in Section 5.

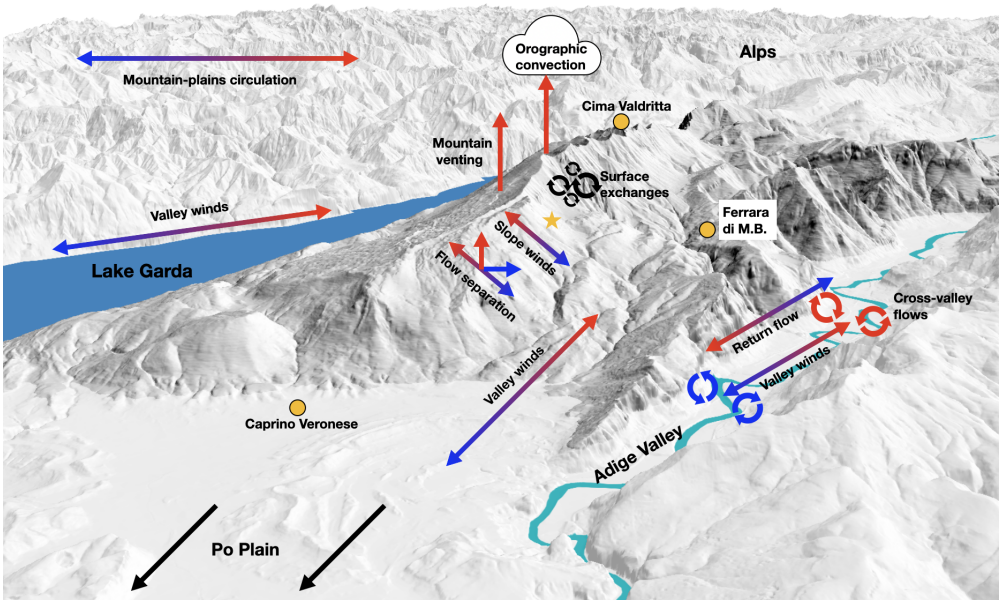


FIG. 1. View of Monte Baldo from the south (orography vertically exaggerated by a factor of 1.2). The red/blue arrows represent thermally driven atmospheric processes characteristic of the study area developing during the day/night. The yellow star indicates the base of the slope.

a.

TEAMx: Multi-scale **t**ransport and **e**xchange processes in the **a**tmosphere over **m**ountains – program and e**x**periment

TEAMx is a bottom-up international research program aimed at advancing the understanding of atmospheric transport and exchange processes over mountainous terrain and assessing how well these processes are represented in numerical weather prediction and climate models (Serafin et al. 2020; Rotach et al. 2022; Lehner et al. 2026). The program brings together research institutions and operational centers and is supported by a coordination office at the University of Innsbruck. Its main scientific objectives are:

- to improve the qualitative and quantitative understanding of transport and exchange between the land surface and the atmosphere, as well as within the atmosphere;
- to evaluate and improve weather and climate models over mountainous terrain;
- to provide a comprehensive observational dataset for investigating a broad range of transport and exchange processes and their spatial and temporal variability;
- to reduce uncertainties in impact models by transferring the resulting knowledge to weather and climate service providers.

The TEAMx observational program comprised a year-long observation period from September 2024 to September 2025, including two intensive observation periods: a winter campaign from 20 January to 28 February 2025 and a summer campaign from 16 June to 27 July 2025.

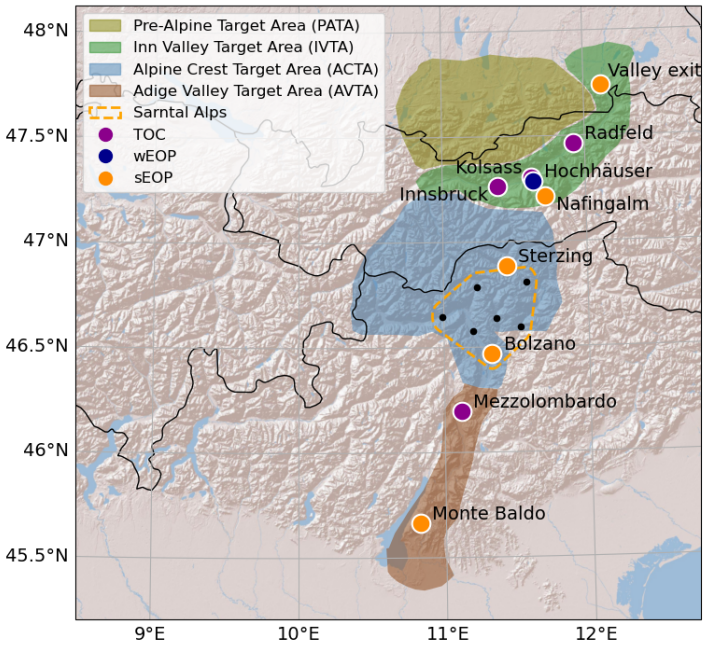


FIG. 2. The target areas for the TEAMx observational campaign. Monte Baldo is located in the southernmost section of the Adige Valley Target Area. Source: Lehner et al. (2026)

1. Target area

Figure 3 presents the location and orographic features of the target area. Monte Baldo is located in the southern Italian Alps and is part of the pre-Alpine range, at the boundary between the Po Plain to the south and the Alps to the north (Fig. 3A).

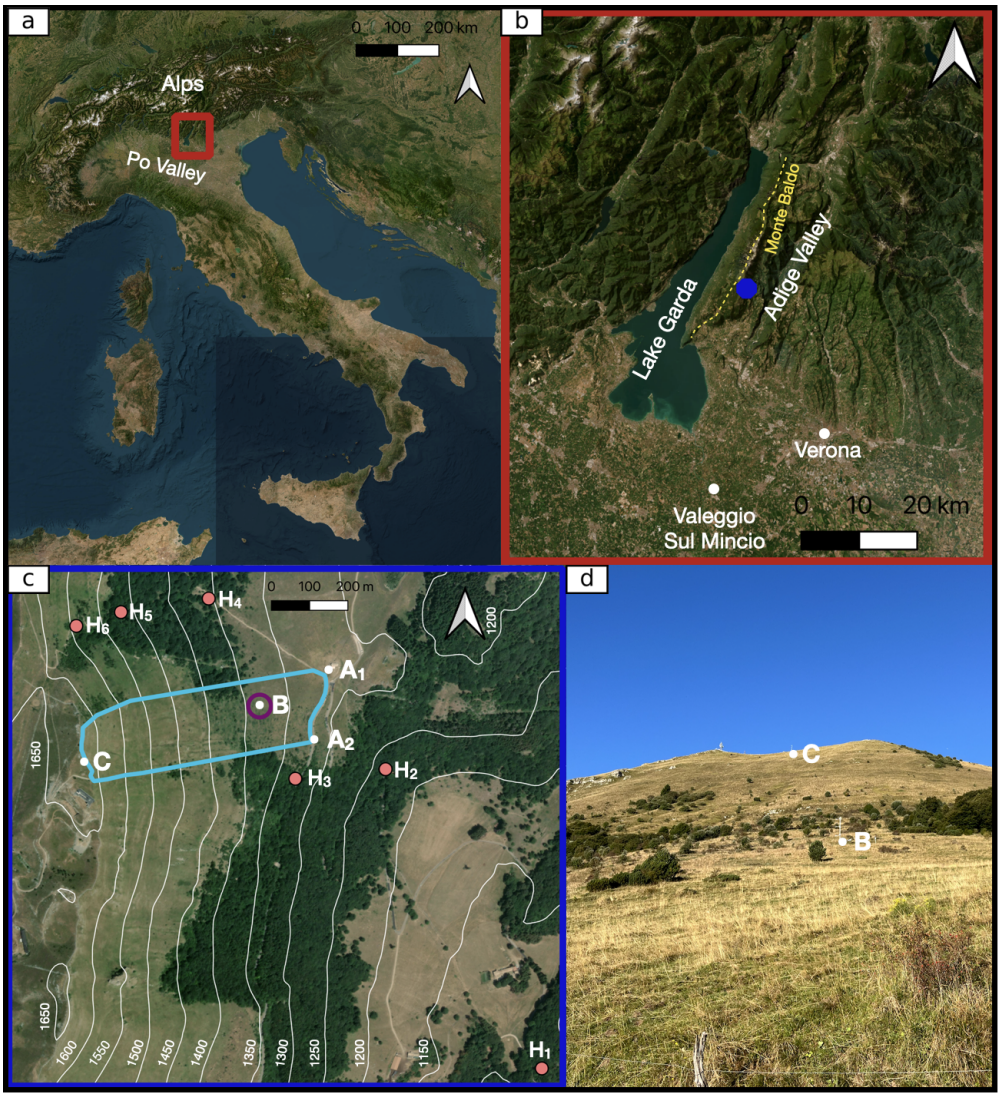
Monte Baldo is a northeast–southwest-oriented mountain range, with its main ridge extending for about 40 km (Fig. 3B). To the east lies the final section of the Adige Valley and its outlet into the Po Plain, which has a canyon-like morphology and is characterized by a valley circulation and a valley exit jet (Giovannini et al. 2017). The Adige River flows through this valley (at about 100 m a.s.l.). To the west lies Lake Garda, extending 370 km^2 to the northeast, which also has a documented thermally driven valley wind system (Laiti et al. 2014; Giovannini et al. 2015). Ranging from 65 m a.s.l. at Lake Garda to 2218 m a.s.l. at its highest peak, Cima Valdritta, Monte Baldo displays a remarkable variety of geographical features and ecosystems, reflected in the presence of diverse economic activities across the area. The target area of the DECIPHER project is located on the southeastern side of the Monte Baldo range, east of the main ridge (blue dot in Fig. 3B).

A detailed overhead view of the target area is shown in Fig. 3C. The white contour lines reveal the regularity of the slope that was the focus of our observational effort. The target slope, highlighted by the azure contours, extends from about 1320 m a.s.l. (point A_1 identifying Malga Valfredda, a mountain hut) to 1680 m a.s.l. (point C, the location of Forte di Naole, an Italian World War I fortress). The average slope within the azure polygon is 29.6° (±6.2°), and the mean aspect is 85.8° (±7.5°). The slope is steeper in the upper part, reaching 35.5° just east of point C, compared with a mean slope of 23.1° (±1.8°) within the violet circle encompassing point B. The values for slope and aspect angles were calculated using the QGIS software and the TINITALY Digital Elevation Model by (Tarquini et al. 2023, 2007).

A picture of the target slope captured from location A_1 (Fig. 1d) reveals that the slope is covered by grass and small shrubs, with beech forest patches to the south and north. This site was selected to identify a topographic setting as simple as possible, ideally characterized by a constant-slope incline. This configuration enables to focus on processes associated with the slope itself, minimizing interference from more complex three-dimensional landforms that may affect both the spatial distribution of incoming radiation and the airflow patterns. To the extent that the target area can be approximated as a tilted plane, all the quantities involved in the process can be expected to exhibit a structure that depends primarily on distance from the ground. Given these characteristics, the target area is ideal to capture and detail slope winds across a range of spatial and temporal scales, together with the associated transport and exchange processes. Its simple geometry also enables a broader transferability of the obtained results to many elementary components of more complex landforms.

2. Observational strategy and instrumental setup

Many different instruments were deployed across the target area and organized into three main observing sites. Malga Valfredda (A_1) served as the base camp for the measurement campaign. It is easily accessible by road and provides useful facilities, including an electrical connection for instrument power supply. All remote-sensing instruments were installed near this site, together with additional instruments for aerosol measurements and ozone observations.



233 FIG. 3. Characterization of the measurement site. (a) Location of Monte Baldo within Italy. (b) Enlarged view
234 of the area outlined by the red rectangle in panel (a), showing Monte Baldo and its surroundings. (c) DECIPHER
235 target area, with measurement sites labeled according to Table 1. (d) Photograph of the slope viewed from site
236 A_1. Basemap: Esri World Imagery, accessed through the QuickMapServices plugin in QGIS. Imagery sources:
237 Esri, Earthstar Geographics, Microsoft, and the GIS User Community.

244 A second observing site was established along the slope (B) to capture slope wind structure,
245 surface-atmosphere exchanges, and aerosol concentrations. Batteries and solar panels provided the
246 necessary power supply to the instrumentation.

Site	Name	Latitude °N	Longitude °E	Elevation m a.s.l.	Site characteristics
A_1	Malga Valfredda, Malga	45.66684	10.82414	1322	Clearing close to the Malga; mostly flat terrain covered by grazed grass and paved surfaces
A_2	Malga Valfredda, roadside	45.66542	10.82369	1316	Roadside close to the Malga
B	Slope	45.66598	10.82183	1383	High grass, approximately 30 cm, and small shrubs, approximately 3 m
C	Forte di Naole	45.66466	10.81606	1668	Crest at the top of the slope; grass with interspersed rocks.
H_1	Eastern slope of Monte Baldo	45.65730	10.83103	1120	Along the road /path; in the canopy of a forest of tall beech/birch trees, approximately 5–15 m
H_2		45.66443	10.82602	1241	
H_3		45.66425	10.82298	1327	
H_4		45.66854	10.82021	1405	
H_5		45.66827	10.81726	1518	
H_6		45.66797	10.81575	1592	
VM	Valeggio sul Mincio	45.35689	10.74199	92	Located in the Po Plain (Fig. 1b)

TABLE 1. Site identifier, location, elevation, and main local surface characteristics of the measurement sites.

Site C was located on the mountain crest in order to investigate the influence of the slope on the "free" atmosphere above peaks. This site, located at Forte di (an old fort, now decommissioned and used for civilian purposes) benefited from both road access and an electrical power supply, supporting more demanding instrumentation, including aerosol and ozone samplers.

In addition to these three main sites, supplementary observations were carried out using distributed thermohygrometers deployed along the road and footpath connecting A_1 to C. The target area was also within the range of an X-band radar permanently operated by the Environmental Protection Agency of the Veneto Region in the Po Plain, located ∼35 km south of the target slope. Figure 4 shows a few selected pictures of the instrumentation deployed in the field at the aforementioned locations.

Tables 2 to 5 summarize the instruments deployed and their periods of operation. The instrumentation can be grouped into four main categories: turbulence and flux measurements, remote-sensing instruments, chemistry and aerosol observations, and supplementary observations.

a. Turbulence and fluxes observational layout

The primary objective of the campaign was to characterize the structure, intensity, and turbulence properties of the thermally driven slope-wind system. For this purpose, several turbulence observations were conducted at the study site, as detailed in Table 2.

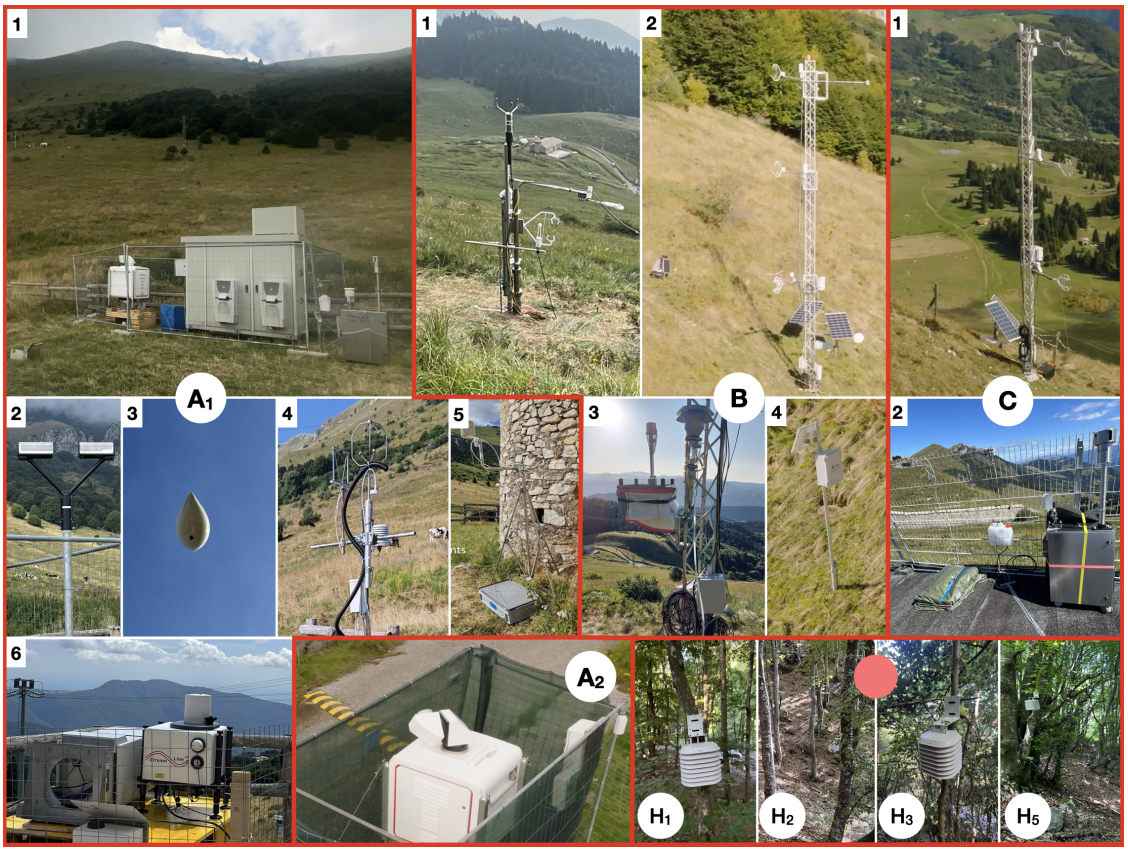


FIG. 4. Site A_1: (1) from the left: Doppler wind lidar (DWL) WINDCUBE 200S, Raman lidar CONCERNING and fine-dust aerosol spectrometer Fidas 200S; (2) Disdrometer OTT-parsivel2 ; (3) tethered balloon; (4) one-level Flux Tower (FT); (5) OPC miniWRAS 1371; (6) From the right: Ceilometer CHM 15k and DWL StreamLine AllSky XR. Site A_2: DWL WINDCUBE 100S. Site B: (1) FT with near-surface profiler; (2) 9-m FT; (3) Optical Particle Sampler (OPS) TSI model 3330 and PQ100 portable ambient particulate sampler; (4) cosmic-ray neutron sensing probe. Site C: (1) 9-m FT; (2) from the right ozone monitor model 205 (covered by green tarp) and fine dust aerosol spectrometer Fidas 200S. Sites $H_{1,2,3,5}$: dataloggers HOBO Pro-v2.

The measurement setup was designed to capture the turbulence structure associated with slope flows and the related surface–atmosphere fluxes at different sites along the slope. The main site was the flux-tower location in B, where a 9-m mast, instrumented at three levels, was installed together with a 2-m mast providing high-frequency near-surface profiling, described in Section 1. Additional soil-moisture and soil-heat-flux measurements were performed to evaluate the surface energy budget along the slope. A 3-m mast was deployed at A_1 to characterize conditions at the foot of the slope, while a 9-m mast was installed at C to capture ridge-top conditions.

Site	Period	Lev.	Height/depth	Instrumentation	Variables – Sampling	Notes
A_1 - FT Malga	21 Jul–22 Oct	1	2.5 m	Thermohygrometer HC2S-L	RH – 1 Hz	With ozone/ozone fluxes observations
			3 m	3-D sonic anemometer uSonic-3 Cape MP	u, v, w, T_s – 10 Hz	
B - FT Slope	10 Jun–9 Oct	soil	-25 cm	Soil moisture and temperature sensor CS655	T_{soil}, q_{soil} – 30 min	
		soil	-15 cm	Soil heat-flux plate HFP01	G_{soil} – 30 min	
		soil	-8 cm	Soil moisture and temperature sensor CS655	T_{soil}, q_{soil} – 30 min	
		1	3 m	3-D sonic anemometer CSAT3A	T_s, u, v, w – 20 Hz	
				open-path analyzer EC150	p, T, [H_2O], [CO_2] – 20 Hz	
		2	6 m	3-D sonic anemometer CSAT3B	u, v, w, T_s – 20 Hz	
				thermohygrometer HMP155	T, RH – 1 min	
		3	9 m	3-D sonic anemometer CSAT3B	u, v, w, T_s – 20 Hz	
				thermohygrometer HMP155	T, RH – 1 min	
				4-way net radiometer NR01	$SW_\downarrow$, $SW_\uparrow$, $LW_\downarrow$, $LW_\uparrow$ – 1 min	
B - FT	17 Jun–26 Jul	1	1.30 m	open-path analyzer LI-COR 7500	p, [H_2O], [CO_2] – 20 Hz	
				3-D sonic anemometer CSAT3B	u, v, w, T_s – 20 Hz.	
			1.60 m	4-way net radiometer CNR2	$SW_\downarrow$, $SW_\uparrow$, $LW_\downarrow$, $LW_\uparrow$ – 1 Hz	
				LW radiometer IR120	T_{surf} – 1 Hz	
				thermohygrometer CS215	T, RH – 1Hz	
				Pressure sensor CS100	p – 1Hz	
		2	2.70 m	2-D sonic anemometer WMT700	u, v – 1 Hz	
			2 mm–2 m	Profiler with thermocouples and Pitot tubes	temperature – 1 Hz and 3D wind-speed profile – 1.5 kHz	See Box 1
C - FT Crest	24 Jun–10 Oct	1	3 m	3-D sonic anemometer CSAT3A	T_s, u, v, w – 50 Hz	
				open-path analyzer EC150	p, T, [H_2O], [CO_2] – 50 Hz	
		2	6 m	3-D sonic anemometer CSAT3B	u, v, w, T_s – 50 Hz	Additional AWS at 9 m – see Table 5
				thermohygrometer HC2S-L	T, RH – 1 min	
		3	9 m	3-D sonic anemometer CSAT3B	u, v, w, T_s – 50 Hz	
				thermohygrometer HC2S-L	T, RH – 1 min	

TABLE 2. Flux-tower and profiler observations, with deployment period. Heights are given relative to the local ground surface; negative values indicate sensor depth below the surface. The column "Lev" indicates measurement levels of fast sensors. Fast- and slow-response instruments are reported together for each measurement level. Here, T_s denotes sonic temperature, T air temperature, T_{surf} surface temperature, [x] the concentration of species x, RH relative humidity, $SW_\downarrow$, $SW_\uparrow$, $LW_\downarrow$, $LW_\uparrow$ are the shortwave (SW) and longwave (LW) upwelling (↑) and downwelling (↓) radiation, G_{soil} the soil heat flux, u, v, w the three components of the wind vector, p pressure and q_{soil} the soil moisture.

b. Remote sensing observational layout

The remote-sensing observations (Table 3) were designed to complement the near-surface measurements performed by instruments installed on the masts. In particular, two DWLs were installed at site A_1 and along the nearby road at site A_2. They carried out coordinated observations of

Site	Period	Instrumentation	Profiled variables	Range–resolution	Notes
A_1	24 Jul–23 Sep	Ceilometer CHM 15k	β	15 km – 15 m	Pointing horizontally towards the Po Plain, southward
	12 Jul–9 Oct	Raman lidar CONCERNING	w_{H_2O}, β, [CO_2]	115 km – 7.5 m	See Box 2 for further details on observed quantities
	13 Jul–21 Oct	DWL WINDCUBE 200S	Radial wind speed	1650 m – 50 m	Scanning routine described in Section b
	24 Jul–23 Sep	DWL StreamLine AllSky XR	Radial wind speed and β	9 km – 3m	Scanning routine described in Section b
A_2	13 Jul–21 Oct	DWL WINDCUBE 100S	Radial wind speed	1650 m – 50 m	Scanning routine described in Section b

TABLE 3. Remote-sensing observations, with β being the aerosol backscatter coefficient, T temperature, w_{H_2O} water vapour mixing ratio and [x] the concentration of species x. The table shows the deployment period, measured variables, range and resolution (in STARE mode for DWL), and additional information for each instrument.

the wind, both by scanning along the slope and by taking vertical profiles. To accomplish this goal, the two coordinated DWLs were programmed to alternate Doppler beam swinging (DBS), plan-position indicator (PPI), and range-height indicator (RHI) scans, in order to characterize both the vertical wind profile and the flow structure along and across the slope. The DBS scans provided vertical profiles of wind speed and direction. The PPI scans sampled radial wind speed in quasi-terrain-following azimuthal slices with increments of 1°, repeated at different elevations between 15° and 45° (with steps of 5°) above the slope. The RHI scans sampled radial wind speed in vertical slices (5°–45° with steps of 1°) aligned with the slope at different azimuths in the following ranges and with steps of 5°. The two lidars were operated with complementary azimuth sectors: one scanned across 250–310° and the other across 210–270°, criss-crossing in the main slope area. Both systems used the same range-gate length (25 m) and sampled ranges from 50 to 1300 m for PPI/RHI scans, while DBS profiles extended from 50 to 1700 m agl. The crossing geometry of the two lidar beams is designed to allow the retrieval of two slope-parallel wind components.

A third DWL was installed at A_1 and set up with a different routine consisting of repeating a 10-min scan schedule with a full cycle during 00:00–12:00 UTC [1] and 13:00–00:00 UTC, and a reduced cycle during 12:00–13:00 UTC. Each 10-min routine during the full cycle included: (i) two Velocity Azimuth Display scans with six azimuth directions (VAD-6) at an elevation of 45°; (ii) two southerly directed RHI scans, pointing toward the Po Plain, at an azimuth of 175°

[1] Coordinated Universal Time. For the region, the Local Standard Time (LST) is UTC+1

and elevations ranging from 0° to 30° in 3° steps; (iii) six RHI scans centered on the mid-slope flux tower, respectively at 240°, 245° and 250° of azimuth and ranging 5°–50° with 5° steps; (vi) two dual-RHI scans at an azimuth of 120° and full-arch elevation from 0° to 170° in 10° steps. The reduced cycle included one VAD-6 scan and only the southerly-directed RHI, with the system operating predominantly in vertical stare mode to facilitate coupling with the Raman Lidar measurements.

A ceilometer was deployed in a southward-facing orientation to assess the transport of pollutants from the Po Plain to the base of the slope, coupled with the southerly-oriented scans of the DWL. Lastly, the Raman lidar CONCERNING (Compact Raman Lidar for Atmospheric CO2 and Thermodynamic Profiling) provided high-resolution, high-frequency vertical profiles of water vapor mixing ratio (w_{H_2O}), CO_2 concentration, and aerosol backscatter coefficient at 0.355 μm. Although temperature measurements were also foreseen, they are not included here due to the poor quality of the corresponding data during the measurement campaign. Further details on this instrument will be provided in Box 2.

Site	Period	Instrumentation	Measured variables	Sampling	Notes
A_1	24 Jul–24 Sep	OPC 11-R	Particle counts in 31 size bins, 0.25–32 μm	6 s	
	10 Jul–22 Aug	OPC miniWRAS 1371	Particle counts in 41 size bins, 0.01–35μm	1 min	
	17 Jul–17 Sep	Fine-dust aerosol spectrometer Fidas 200S	Particle counts in 256 size bins, upper bin borders 0.147–17.64 μm	2 min	Also provides derived PM_1, $PM_{2.5}$, PM_4, PM_{10}, T, T_d, RH and p
	17 Jul–10 Oct	Low-cost OPC	PM_1, $PM_{2.5}$, and PM_{10}	20 s	Developed by the Institute of Polar Sciences.
	10 Jul–22 Oct	Ozone monitor model 205	[O_3]	30 min	
	21 Jul–22 Oct	Fast chemiluminescence O_3 analyser	[O_3]	10 Hz	Used with sonic-anemometer data for ozone-flux estimates
B	17 Jul–10 Oct	Low-cost optical particle counter	PM_1, $PM_{2.5}$, and PM_{10}	20 s	Developed by the Institute of Polar Sciences. Sensing device: Plantower PMS5003.
	25 Jun–4 Jul 9 Sep–16 Sep	PQ100 portable ambient particulate sampler	Ice-nucleating particles (INPs)	1 h 55 min accumulation time	
	24 Jun–8 Jul	OPS TSI model 3330	Particle counts in 16 size bins, 0.3–10 μm	10 min	
C	17 Jul–9 Oct	Fine-dust aerosol spectrometer Fidas 200S	Particle counts in 256 size bins, upper bin borders 0.147–17.64 μm	2 min	Also provides derived PM_1, $PM_{2.5}$, PM_4, PM_{10}, T, T_d, RH and p
	17 Jul–9 Oct	Low-cost optical particle counter	PM_1, $PM_{2.5}$, and PM_{10}	20 s	Developed by the Institute of Polar Sciences. Sensing device: Plantower PMS5003.
	22 Aug–9 Oct	Ozone monitor model 205	[O_3]	30 min	

TABLE 4. Overview of ozone and aerosol particle measurements. For each instrument, the table shows the deployment periods, instruments, measured variables, sampling period or frequency, and additional information. For aerosol spectrometers and optical particle counters, particle-count measurements are reported along with the number of size bins and, where available, the nominal lower and upper size limits.

c. Aerosols and chemistry

Besides meteorological variables, instruments measuring the atmospheric particulate matter (PM) load at different sites were deployed (see Table 4). The distribution of the PM sensors was designed to capture the variability along the slope of aerosol concentrations and to assess possible contributions from slope-wind-driven transport, particularly during daytime anabatic conditions. These surface-based observations were complemented by remote-sensing measurements of aerosol backscatter coefficient. Furthermore, sensing systems integrating commercially available low-cost sensors were co-located with state-of-the-art instruments for real-time PM concentration measurements to evaluate the sensor performance, develop calibration and correction models, assess model robustness, and investigate their suitability for the future deployment of sensor

networks in remote Alpine regions. In addition to investigating PM load, Ice Nucleating Particle (INP) concentrations were evaluated from samples collected on filters during 18 campaign days at site B. Measurements aimed to quantify INP transport to the mountain crest in the presence of thermally driven mountain venting. A remarkable aspect of the campaign was the investigation of ozone concentrations and fluxes, for which datasets from intensive observation campaigns in complex terrain remain scarce in the community (see Box 2).

Site	Period	Instrumentation	Measured variables	Sampling	Notes
H_1–H_6	19 Jun–10 Oct	Six thermohygrometers and dataloggers HOBO Pro-v2	T, RH	10 min	Installed 2 m a.g.l. within the forest canopy along the slope
A	25 Jul–24 Sep	Disdrometer OTT-parsivel2	diameter and velocity of precipitating particles	1 min	
	24 Jun–27 Aug	AWS WXT 530	T, RH, p, precipitation, u, v	5 min	
	17 Jun–8 Jul	Tethered balloon	T, RH, p, horizontal wind speed	30 min	Range: 5–120 m, 5 m steps.
B	8 Aug–9 Oct	Cosmic-ray neutron sensing probe	Muon and neutron counts, p, gravimetric and volumetric q_{soil}	1 h	See Box 3
C	24 Jun–9 Oct	AWS ATMOS 41 Gen2	T, RH, p, u, v, lightning counts and distance, precipitation, $SW_{\downarrow}$	5 min	At the top of the 9 m EC tower
VM	Operational	X-band weather radar WR-10X	Reflectivity	5 min	Operated by ARPAV, 6 elevations.

TABLE 5. Additional meteorological and environmental observations. The table reports the deployment period, instrumentation, measured variables, sampling period or frequency, and additional information for each instrument.

d. Complementary observations

A number of complementary observations were also performed during the campaign. These observations, summarized in Table 5, include measurements of precipitation and convective activity (reflectivity and lightning) from automatic weather stations, a disdrometer, and a radar; distributed soil moisture from a cosmic-ray neutron sensor (detailed in Section 2); temperature and relative humidity within the forest canopy along the slope from stand-alone thermohygrometers. During the first part of the campaign, a tethered balloon was also operated to characterize ambient stratification. These instruments were either already operational before the campaign (e.g. the ARPAV X-band radar), or specifically deployed for the campaign period. The campaign also benefited from AWS and air-quality stations from the ARPAV network, local institutions, and mountain refuges, which are not reported in the table.

e. Special observations box: Description of selected special observations during the campaign

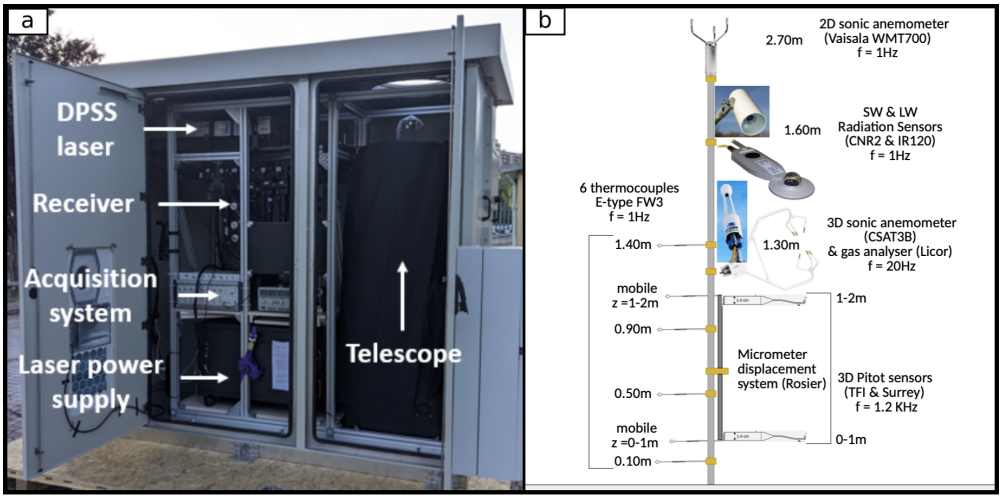


FIG. 5. (a) Raman lidar CONCERNING; (b) scheme of the near-surface profiling setup.

1) NEAR-SURFACE PROFILING

An in-situ atmospheric measurement system was deployed at site B for studying the near-surface turbulent boundary layer in thermally driven slope winds. It uses two multi-hole 3D Pitot probes mounted on a high-precision vertical micrometer displacement system to sample the slope-parallel wind speed at high frequency (more than 1 kHz), from about 2 mm above the ground up to 2 m. The Pitot sensors operate in conjunction with thermocouples, which characterize the near-surface temperature profiles and complement the velocity measurements obtained during the profiling

period. Near-surface measurements were collected as one-minute samples at 30 vertical positions between 2 mm and 1 m above the ground. The measurement positions were regularly distributed on a logarithmic scale, providing greater resolution close to the surface. A second Pitot sensor similarly profiled the layer between 1 and 2 m. A complete vertical profile took approximately 30 minutes. Measurements were conducted in the morning during anabatic-flow episodes and in the evening during katabatic-flow episodes (Fig. 7, gray vertical bands). A sonic anemometer mounted at a height of 1.30 m provided continuous reference measurements of three-dimensional wind velocity and temperature. Surface temperature was derived from longwave infrared radiation measured with an IR120 infrared radiometer. These observations fill a measurement gap very close to the ground that is usually not reached by conventional instruments, and they aim to improve wall-law formulations and surface boundary conditions for numerical simulations over sloping terrain. The present set-up is the first to be used in mountainous terrain to resolve the turbulent boundary layer down to the roughness layer very close to the surface.

2) Raman lidar CONCERNING

CONCERNING (COmpact RamaN lidar for atmospheric CO_2 and thERmodyNamic profilING) is a ground-based Raman lidar designed to provide high-resolution vertical profiles of the two main atmospheric greenhouse gases, CO_2 and water vapor, together with temperature and particle backscatter, extinction, and depolarization, from near the surface up into the mid atmosphere (Di Girolamo et al. 2023; Di Paolantonio et al. 2026). This multi-variable profiling capability makes it a key tool for disentangling local processes and larger-scale transport: by resolving how atmospheric structures evolve with height and time, CONCERNING can distinguish local signatures from those of the free-tropospheric background. Its high temporal and vertical resolution also enables the resolution of turbulent fluctuations in the profiled quantities, opening the possibility of retrieving vertical fluxes when combined with collocated, vertically pointing DWLs. During DECIPHER, the system was installed at A_1, providing continuous, high-resolution night- and daytime profiling of variables in support of the campaign's objectives.

3. Overview of the campaign and observed conditions

a. Meteorological overview and comparison with climatology

Fig. 6 provides an overview of the observed daily mean temperature and daily accumulated precipitation, compared with their counterparts from ERA5-Land hourly data (Muñoz Sabater 2019). The latter includes the climatological mean and variability in the 5^{th}–95^{th} percentile range for the period 1996-2025 for the target area, after the interpolation of the four closest grid points. Observed lightning strikes within 5 km of site C are also reported alongside daily precipitation in panel b. To account for the different elevations of the true ground and the ground-level computed by ERA5, the air temperature from ERA5 is corrected to the true elevation using the standard atmospheric lapse rate (6.5 K km^{-1}).

Overall, ERA5 agrees well with the temperature observations. For precipitation, the differences are more pronounced, with ERA5 showing more precipitation events than the observations[2].

June began with above-average temperatures, which exceeded the 95th percentile toward the beginning of July. During the first decade of July, a weather shift occurred, with several precipitation and convective events with lightning and temperatures at or below the climatological average. These unsettled conditions persisted until 8 August, when a period of stable weather began. Fair weather lasted until August 15, when a further unsettled phase opened up, characterized by lower-than-average temperatures and frequent convective events up to the first days of September. From then until the end of the campaign in mid-October, only very few fair-weather days were observed.

A similar analysis considering CAMS data (Inness et al. 2019) and particulate matter and ozone observations, reported in Appendix A, reveals that these wet and unsettled conditions resulted in climatologically low PM loadings and ozone concentrations, with only a few episodic enhancements during fair weather conditions.

b. Slope wind hours

Fig. 6c shows the hours during which the conditions were conducive to the development of thermally driven winds. The flag is obtained from a multi-factor criterion considering the homogeneity of the large-scale pressure field, cloud coverage and precipitation, and weak synoptic

[2]Precipitation observations are only available from 24 June onward.

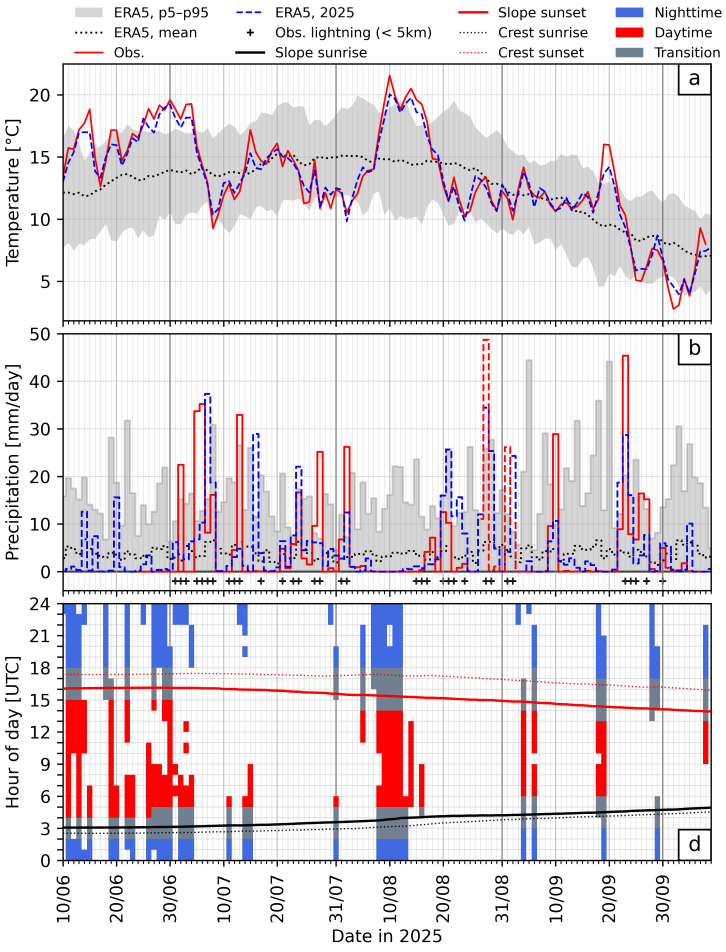


FIG. 6. Overview of meteorological conditions during the campaign and comparison with climatology. Temperature (a) is measured at the 3 m level along the slope, (b) precipitation and lightning are obtained from the ATMOS 41 weather station (full red line) and disdrometer measurements (dashed red line), and (c) slope wind hours with local sunrise and sunset times for sites B (full lines) and C (dotted lines).

forcing. These conditions and the description of the calculation of the flag values are reported in Appendix B.

A total of 572 hours, corresponding to 18.5% of the campaign, can be considered conducive to the study of slope winds and related processes. This suggests that field campaigns aimed at studying slope winds should be sufficiently long to maximize the likelihood of observing suitable conditions.

4. Overview of selected results from the campaign

a. Multi-platform observations of slope winds

To address the multi-scale nature of slope winds, a multi-platform observational system is used to extract and detail the dynamic characteristics of anabatic and katabatic flow events. Specifically, a multi-sensor profile is "built" at site B location, combining the near-surface profiling system and the flux tower with the extrapolated velocity from the DWLs WINDCUBE at site A_1 and A_2. This combination ensures the reconstruction of the wind profile up to approximately 100 m while detailing its near-surface characteristics. Near-surface turbulent exchanges and flow evolution are therefore captured with high temporal and vertical resolution, and coupled with upper-air flow evolution and vertical perturbations.

In the following sections, the reconstruction of the vertical profile is described, together with an application to anabatic and katabatic events respectively on the 14th and 15th of July, corresponding to conditions suitable for the development of slope winds.

1) The multi-sensor profile

Preliminary data processing is applied independently to measurements from the profiler, flux tower, and DWLs. The Pitot-tube data from the profiler were despiked, grouped by elevations, and averaged to obtain a 60-point profile covering 30 minutes with a higher sampling rate at the surface (see, for instance, Obligado et al. 2022; Charrondière et al. 2022b). Sonic anemometers from the flux tower were despiked according to Vickers and Mahrt (1997) over 30-min windows, and outliers were replaced through linear interpolation. RHI scans from DWLs were first screened using a cut-off threshold on the carrier-to-noise ratio of 15 dBz to avoid saturated backscatter signals; afterwards, a moving window filter was applied to identify poor measurements and replace them with linearly interpolated values from the same scan, following Menke et al. (2020).

A dual strategy on DWL data was implemented to reconstruct the most representative profile for the current slope: first, the RHI scan at 292° of azimuth, pointing at the exact flux tower location in site B, is considered for validation (namely AZ292); the profile is reconstructed geometrically and interpolated among range gates to the exact location of the flux tower to enhance the comparability; then, the RHI scan at 268° of azimuth aligned to the direction of the slope aspect is used to assess the multi-sensor profile of the slope wind (namely AZ268). In this second case, the profile

is reconstructed geometrically, but data are averaged over a 200 m segment across the flux tower location (corresponding to 4 range gates). The latter choice is motivated by the aim of reconstructing the slope wind profile where it is expected to form, in accordance with the slope's geometry. With the reasonable assumption of horizontal homogeneity along the slope (away from the slope crest and bottom), the slope wind is expected to be independent of the cross-wind direction. Moreover, given the regularity of the slope, along-slope variability in the wind speed should also be small. Therefore, the flow in the slope-wise direction is reasonably similar at the flux tower in site B and at each point of the slope with a comparable elevation, i.e., where the DWL is pointing. These assumptions are corroborated by the full range of variability of the RHI scans across all azimuths in the range-gate interval of interest, which is contained within approximately 1.5 times the instrumental error (0.5 ms^{-1}).

As mentioned, the AZ292 was meant for validating the DWLs velocity with that of the flux tower, as shown in Fig. 7a.

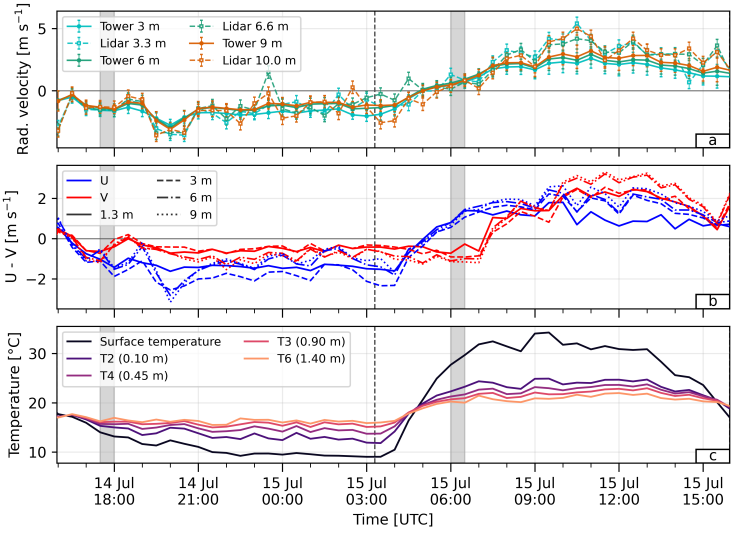


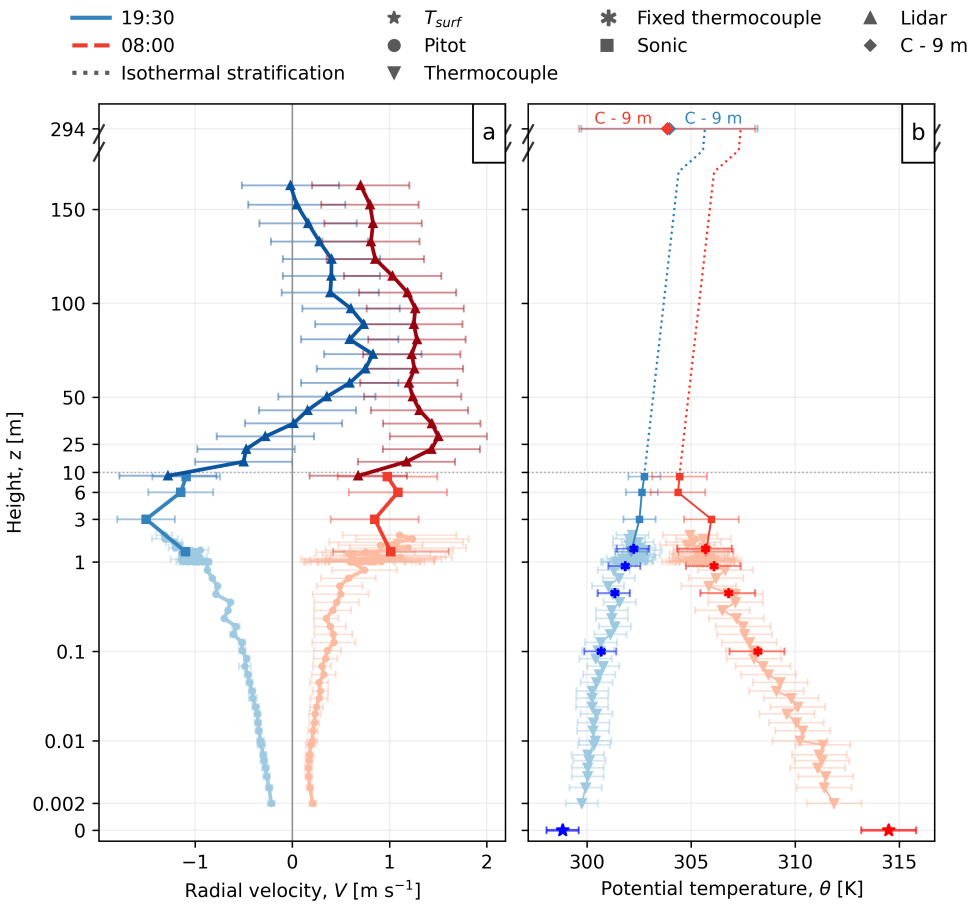
FIG. 7. (a) Comparison of radial velocity from the DWL at site A_2 and the flux tower at location B. Error bars are the propagated errors on the flux tower measurements and the instrumental error for the DWL. (b) Time series of slope-parallel and across-slope wind components for the 14 and 15 of July as observed by the sonic anemometers at location B, together with (c) temperature observations from fixed thermocouples mounted on the 3-m mast and surface temperature from the IR120 radiometer. The shaded areas highlight the operational period of the profiler.

For this purpose, the wind components measured with the sonic anemometers are converted into radial velocity following Bonin et al. (2017). Despite the agreement among sensors, the DWLs' time series show several missing data points owing to a mix of low-quality measurements and a "clean" atmosphere. In fact, the drawback of adopting a DWL away from sources of particulate matter is the lack of solid atmospheric constituents for backscattering, resulting in periods of missing data. Compared to quality-check methods based entirely on the carrier-to-noise ratio, the Menke et al. (2020) algorithm guarantees a larger data sample, but it cannot save valuable data points when the entire scan is of low quality. This seems to apply more to the DWL in site A_1 (not shown), which will not be used in the case-study analysis, since it falls within low-quality-data windows for this instrument. As a drawback, the analysis is performed entirely in radial velocity rather than in true wind components. It is worth noting, however, that in pure slope wind conditions, the radial velocity in the slope aspect direction is similar to the true wind speed.

2) A case study of anabatic and katabatic winds

Figure 8 shows the multi-sensor profile of radial velocity and potential temperature for the katabatic wind episode starting at 1730 UTC on July 14th and the anabatic wind episode at 0600 UTC on July 15th.

Following the same procedure applied to the data from sonic anemometers, the profiler wind components are first converted into radial velocities. For the computation of potential temperatures, the atmospheric pressure profile is determined from measurements at 1.3 and 3 m and extrapolated recursively using the hypsometric equation. At the surface below 2 m, air temperature is measured using a set of thermocouples mounted on the profiler, while along the Flux tower in B, air temperature is measured with sonic anemometers and thermo-hygrometers up to 9 m height. The vertical profile is complemented by the temperature measured at the 9-m level of the flux tower in C, reported at 294 m, accounting for the elevation difference between the two flux towers. The ambient stratification above 9 m is expected to consist of a weakly stratified layer with a corresponding Brunt-Väisälä frequency $N = \sqrt{\gamma - 1}g/c = 0.018$ s^{-1} (where $\gamma = 1.4$, g is the acceleration due to gravity, and c is the speed of sound) consistent with typical quasi-isothermal conditions as observed in slope flow configurations (e.g. Charrondière et al. 2022b). It is presently reported in Figure 8b as a dashed line and shows a trend consistent with the two upper measurements at 6 and 9 m, and



492 FIG. 8. Multi-sensor profile of radial velocity (a) and potential temperature (b) for the katabatic wind episode
493 starting at 1730 UTC on July 14th and the anabatic wind episode at 0600 UTC on July 15th. The slope of the
494 dashed lines, representing isothermal stratification, is respectively 10.2 and 10.3 K km^{-1} for the katabatic and
495 anabatic cases, and they were calculated considering observations at the 9 m level at site B.

512 the 294-m temperature from the flux tower in C, both for the katabatic and for the anabatic wind
513 temperature profiles.

514 The profiler can only sample winds aligned with the direction of the Pitot probe. Hence, the
515 observed episodes have been focused on the morning and evening transitions, when interfering
516 valley winds (blowing spanwise to the slope winds) are weak. Therefore, the shape of the profiles
517 in Fig. 8a is not yet the typical slope wind characterized by a well-developed jet and a decoupling
518 from larger-scale flows, if no entrainment is observed. Nonetheless, some significant features are
519 already captured: the katabatic wind profile has already developed a preliminary jet shape, with a

maximum in radial velocity around 3 m, consistent with findings from similar studies of katabatic jets on grass-covered slopes (e.g., Charrondiere et al. 2020). Above 40 m, the radial velocity changes sign, revealing the persistence of an upslope flow from the late afternoon. During the daytime, the wind is already flowing upslope, and a jet-like shape is starting to form, despite the low radial velocities. A weak jet maximum appears around 25 m, but its development is not yet clear. The addition of second-order moments and turbulent kinetic energy will help clarify the profiles and better locate a possible jet maximum, but this is beyond the scope of this initial analysis, which is intended to showcase a preliminary use of such a complex instrumentation setup.

The profiles of potential temperature in Fig. 8b appear symmetrical in both episodes, consistent with typical boundary-layer characteristics. During the daytime, strong incoming solar radiation at the surface generates a similarly intense vertical temperature gradient, especially in the first meter. During the nighttime, the thermal inversion creates a similar temperature gradient, although less steep. Both profiles appear to converge toward a weakly stratified layer consistent with near-isothermal conditions, under which potential temperature increases by approximately 10 $\mathrm{K\,km^{-1}}$. For the katabatic wind episode, where the regime seems more developed, the jet maximum corresponds roughly to the elevation at which the potential temperature profile changes gradient, evolving towards isothermal conditions. The same conclusion cannot be inferred for the anabatic wind profile either, because the location of the jet maximum (if any) is less precisely detectable.

Overall, this exercise allowed us to showcase a preliminary application of the multi-platform observation system: to the best of our knowledge, this is a first attempt in complex terrain to integrate ground-based remote sensing measurements with the high-resolution (spatial and temporal) data of a profiler system designed to detail the near-wall region of the inner turbulent boundary layer. The presence of a transient flow scale accessible to the sonic anemometers facilitates merging, thereby enlarging the possibilities for future investigations.

---

3) Box: Cosmic ray neutrons to measure soil moisture

Monitoring soil moisture, soil temperature, and ground heat flux is essential for characterizing the surface energy budget and soil–atmosphere exchange processes. Conventional probes, however, provide pointwise measurements. To insert them, one may need to dig, thereby modifying the soil. The above issues limit their spatial representativeness.

To complement conventional soil moisture measurements, a Finapp Model F3 Cosmic-Ray Neutron Sensor (CRNS) was deployed at site B, providing continuous, non-invasive estimates of area-integrated soil moisture. Unlike point sensors, the CRNS samples a footprint with a radius of approximately 100–250 m (Fig. 9a) and an effective sensing depth of up to ~50 cm, depending on soil and moisture conditions. This intermediate spatial scale helps bridge the gap between local in situ observations and satellite remote sensing products.

The sensor detects secondary cosmic-ray neutrons using a ^{6}Li-based scintillation detector coupled to optical light guides and a photomultiplier tube (PMT). Neutron intensity is inversely related to soil water content (Zreda et al. 2008; Gianessi et al. 2024). At site B, CRNS observations were compared with point soil-moisture sensors installed at different depths (Fig. 9b). The different datasets show consistent temporal variability and coherent responses to precipitation events.

The compact, low-power design of the Finapp F3 also enables autonomous solar-powered operation, making it suitable for long-term deployment in remote environments. These observations supported the investigation of land–atmosphere coupling and the role of soil moisture in thermally driven winds.

b. Following the pollution: multi-instrumental observation of thermally driven aerosol transport from plains to mountain crest.

Observations on 9 August 2025 show how regional advection and thermally driven slope winds transported aerosol-rich air from the Po Plain toward the Monte Baldo crest through site A_1. The event occurred under conditions conducive to the undisturbed development of the thermally driven wind system (Fig. 6d). Coordinated measurements from the StreamLine XR DWL, the southward-pointing ceilometer CHM 15K, together with the in-situ characterization of PM10, wind speed and direction, temperature, relative humidity, and radiative fluxes captured the regional inflow, local slope circulation, and aerosol response over a complete diurnal cycle.

1) Diurnal evolution and southerly aerosol inflow.

Vertical-stare DWL and Raman lidar measurements showed weak aerosol backscatter during the night and early morning, mainly within a shallow surface layer (Fig. 10a). From 0800 UTC, backscatter increased and an aerosol- and water-vapour-rich mixed layer, hereafter MAL, developed above the site. During late morning and early afternoon, the MAL deepened to approximately

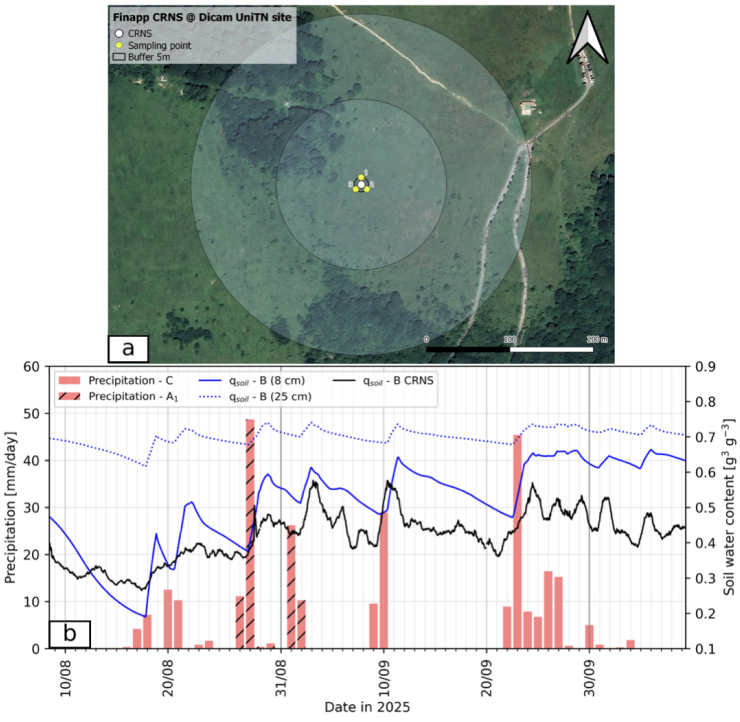


FIG. 9. Panel a: footprint of the Finapp CRNS probe around site B. Panel b: gravimetric soil moisture observations from CRNS and soil sensors at site B, with daily accumulated precipitation.

600 m above the DWL, reaching an upper boundary of 1900 m a.s.l., above C. This demonstrates that the MAL was sufficiently deep to engulf the crest. After 1400 UTC, the MAL became less homogeneous and progressively shallower. A secondary near-surface backscatter enhancement occurred during late afternoon before the MAL collapsed rapidly around 1900 UTC, with the intrusion of dry and aerosol-free air from the free troposphere. Only shallow and intermittent aerosol layers remained during the evening. Vertical Doppler velocities indicated daytime motions within the MAL, but no persistent upward flow over A_1 (Fig. 10b). Descending velocities frequently occurred during the mature phase of the anabatic circulation. The absence of sustained ascent during the initial development of the PBL suggests that vertical aerosol transport was not dominated by direct vertical lifting above the site. Instead, the observations point toward a predominantly terrain-following pathway, while the vertical scans above A_1 sampled turbulence and compensating motions within the MoBL. Wind profile retrievals from VAD scans (Fig. 10cd) showed predominantly southerly low-level winds in the morning and in the central part of the day, consistent with the arrival of air from the Po Plain. Westerly winds prevailed above the southerly

inflow, indicating a vertically differentiated circulation and a possible compensating return branch or large-scale wind. During the afternoon, the southerly inflow weakened and shifted progressively toward the northeast as the MAL began to break down, indicating that the MAL breakup closely follows the local circulation transition and reorganization. Southward-looking DWL and ceilometer measurements provided evidence of the aerosol pathway. Negative radial velocities observed by the DWL beam pointed towards an azimuth of 175° revealed a persistent southerly flow toward A_1 throughout the daytime aerosol enhancement (Fig. 11b). Concurrently, the ceilometer detected aerosol-rich air over several kilometers south of the observing site (Fig. 11c). Around 1900 UTC, the backscatter signal weakened and detached filaments appeared, indicating the collapse of the organized daytime transport pathway. The combined observations are consistent with a daytime southerly up-valley flow transporting aerosol-rich air from the Po Plain sector through the lower Adige Valley toward A_1, lasting mainly from 08 UTC until 16 UTC.

Along-slope transport processes and coupling with measurements at the crest.

Dual azimuth RHI scans showed how aerosol-rich air reaching A_1 was redistributed along the mountain flank by the slope-wind system. Opposite scans, with azimuths of 300° and 120° pointing respectively toward the upper Monte Baldo slope and the Adige Valley, were oriented in the direction of the dominant slope-wind axis as observed by the along-slope flux tower (Fig. 12a). At 0209 UTC, the lidar observed the downslope flow accompanied by weak aerosol backscatter (Fig. 13a). By 0709 UTC, the circulation had reversed and a terrain-following upslope current was established (Fig. 13b). At 1039 UTC (Fig. 13c), a deep and organized anabatic flow extended from the lower slope toward the crest, while enhanced aerosol backscatter occupied approximately the same volume. This collocation directly links the anabatic circulation to aerosol transport. A descending branch above the main slope current, together with westerly flow aloft at site A_1, was consistent with compensating or partially recirculating motion. In situ PM10 measurements (Fig. 12d) further demonstrated coupling between sites A_1 and C. From morning through early afternoon, concentrations at both sites increased from approximately 10 to 20-25 $\mu g\,m^{-3}$ and evolved in close agreement. This occurred while the MAL extended above C and the lidar showed a deep terrain-following current. The PM records diverged during the late-afternoon decay (between 17 and 18 UTC), with PM10 at site C decreasing earlier and more abruptly while PM

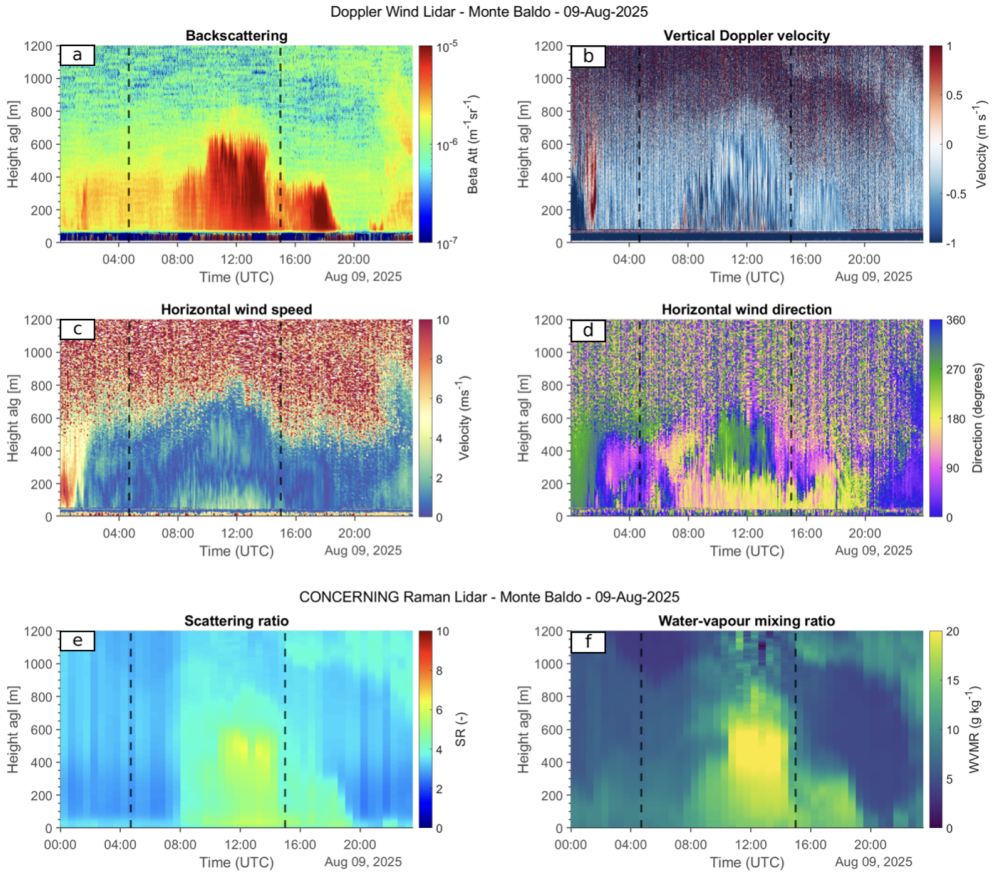
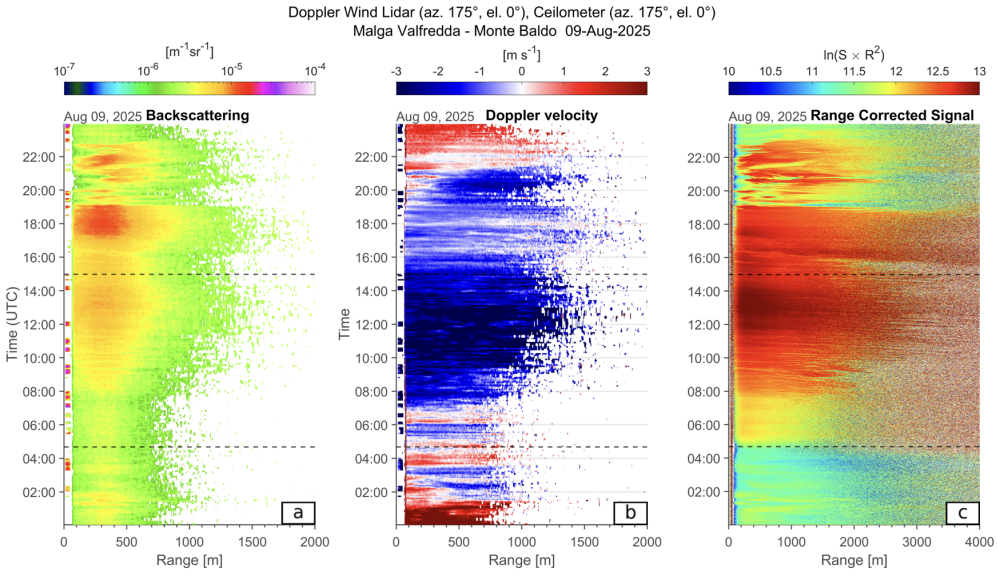


FIG. 10. Diurnal evolution of the aerosol layers, wind, and specific humidity above A_1 on 9 August 2025, observed with the StreamLine XR Doppler wind lidar and the CONCERNING Raman lidar. (a) Attenuated backscatter coefficient and (b) vertical Doppler velocity from vertically pointing STARE measurements. (c) Horizontal wind speed and (d) meteorological wind direction retrieved from VAD scans at an elevation angle of 45°. (e) Scattering ratio (f) and water-vapour mixing ratio from Raman lidar measurements. The dashed vertical lines in the plots mark local sunrise and sunset times. **labels, check caption order**

loadings remained elevated for longer at site A_1. As the MAL collapsed, the higher site exited the aerosol-rich layer earlier than the lower site.

Radiative control, evening transition, and transport timescales.

The late-afternoon transition highlights the close coupling between surface heating, slope winds, and MAL depth. Net shortwave radiation peaked near local noon and declined during the afternoon before dropping sharply at about 1600 UTC, when the east-facing Monte Baldo slope entered shadow (Fig. 12c). This coincided with a rapid temperature decrease at A_1, a rise in relative

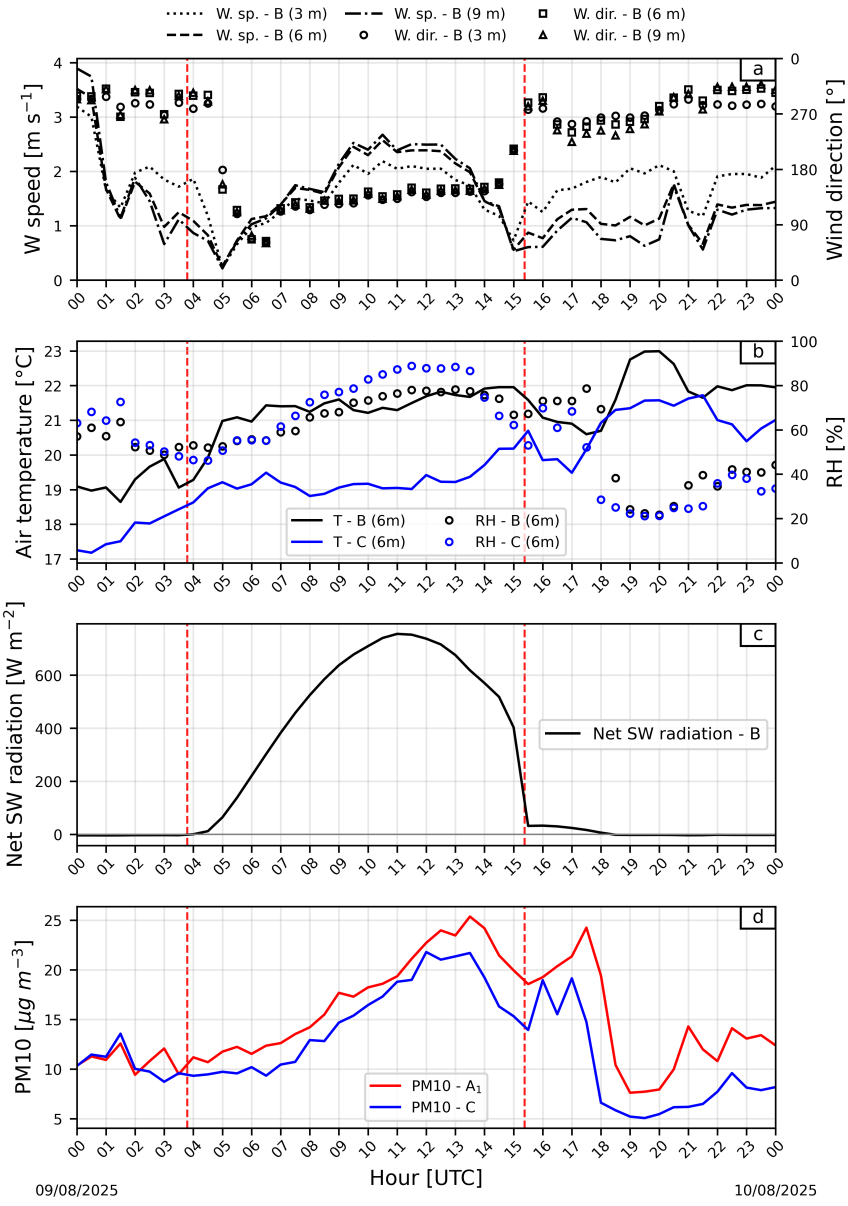


583 FIG. 11. Time–range evolution of aerosol and radial wind along the southern transect from A_1 toward the
584 Adige Valley outlet and Po Plain sector on 9 August 2025. (a) Attenuated aerosol backscatter measured by the
585 StreamLine XR Doppler wind lidar along a near-horizontal beam at an azimuth of 175° and an elevation angle of
586 0°. (b) Corresponding radial Doppler velocity; negative values indicate air moving toward A_1 from the southern
587 sector, whereas positive values indicate motion away from the site toward the lower slope. (c) Range-corrected
588 signal measured by the horizontally pointing CHM 15K ceilometer along approximately the same direction. The
589 dashed horizontal lines in the plots mark local sunrise and sunset times.

656 humidity from about 70% to nearly 90%, and a weakening of the upslope anabatic circulation
657 (Fig. 12a,b).

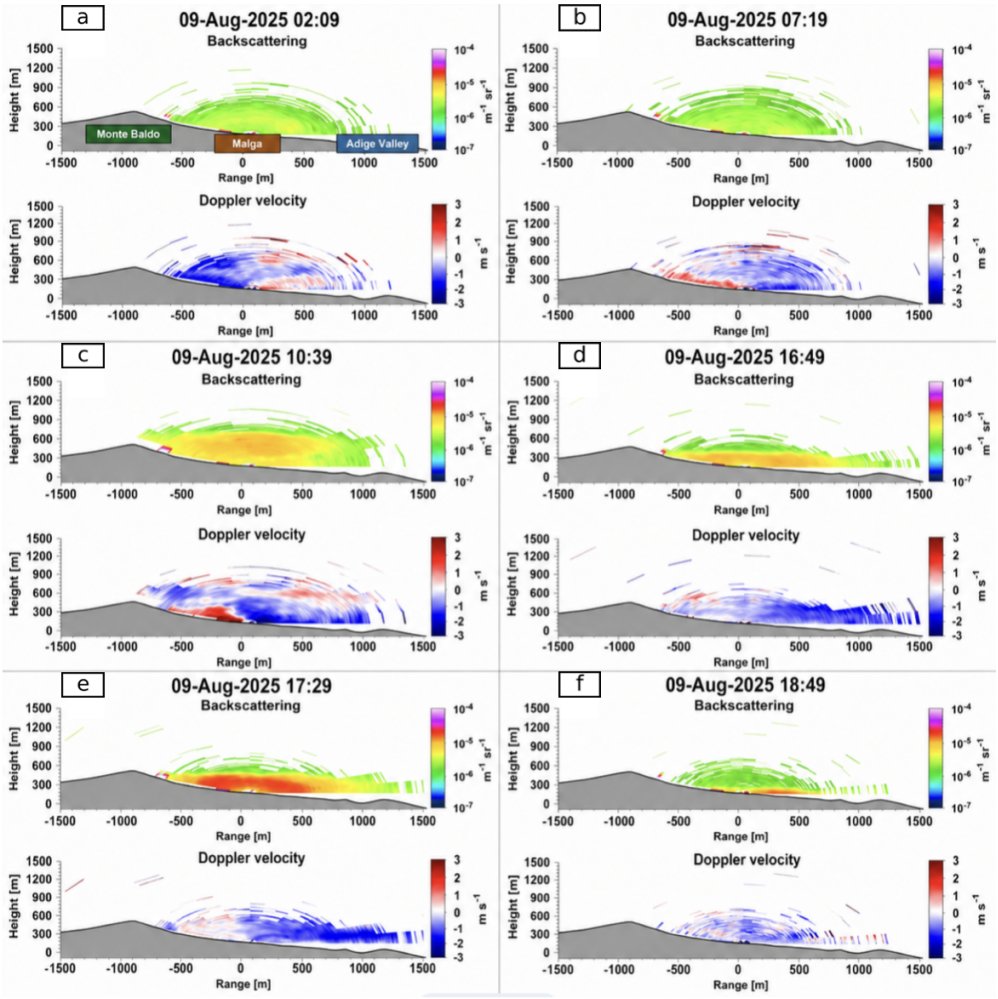
658 Accordingly, the 1649 UTC RHI scan showed a weaker up-slope current and a shallower MAL
659 (Fig. 13d). Backscatter then increased markedly at 1729 UTC despite the weakened circulation
660 (Fig. 13e). This enhancement, also observed by the southward-pointing DWL and ceilometer,
661 likely resulted from aerosol accumulation within the lowering layer and hygroscopic growth under
662 high humidity. By 1849 UTC, the aerosol-rich layer had descended substantially and no longer
663 reached C across most of the observed section (Fig. 13f). Around 1900 UTC, the continuous
664 structure disappeared, leaving only detached aerosol features and marking the end of the daytime
665 connection between the lower slope and the crest.

666 The observations also provide characteristic transport timescales. The upslope circulation de-
667 veloped from 0719 to 1039 UTC, reaching a mature aerosol-laden state within about 3 h. After



621 FIG. 12. Timeseries for 9 August 2025 of 30-min averages of (a) wind speed and direction at the three levels
622 of the FT in site B, (b) T and RH from the Fidas 200s instruments at site A_1 and at site C, (c) Net shortwave
623 radiative flux measured at site B and (d) PM10 mass loadings at site A_1 and at site C. The dashed vertical lines
624 in the plots mark local sunrise and sunset times.

668 shortwave forcing collapsed near 1600 UTC, the slope current weakened within less than 1 h.
669 The MAL then lowered and fragmented over the following 2 h, disappearing by 1849–1900 UTC.



625 FIG. 13. Selected dual-azimuth RHI cross sections collected by the StreamLine XR Doppler wind lidar at site
626 A_1 on 9 August 2025. The scans were performed along opposite azimuths of 300° and 120°, approximately
627 aligned with the principal slope axis and directed toward the upper Monte Baldo slope and the Adige Valley,
628 respectively. For each time frame, the upper panel shows attenuated aerosol backscatter and the lower panel shows
629 radial Doppler velocity; the grey area represents the underlying terrain. Panels correspond to (a) 0209 UTC, (b)
630 0719 UTC, (c) 1039 UTC, (d) 1649 UTC, (e) 1729 UTC, and (f) 1849 UTC. The sequence captures nocturnal
631 downslope drainage, the establishment and mature development of an aerosol-laden upslope circulation, and its
632 late-afternoon weakening, lowering, and fragmentation.

670 Overall, coherent aerosol transport lasted about 11 h, from the first marked backscatter increase
671 near 0800 UTC to the evening breakdown around 1900 UTC.

This sequence shows how daytime southerly up-valley flow transported aerosol-rich air from the Po Plain through the lower Adige Valley, while anabatic circulation redistributed it upslope to C. The loss of solar heating then weakened the slope wind, causing the MAL to descend and fragment.

---

2) Ozone in the mountains

Ozone (O_3) flux measurements provide a complementary perspective on the vertical transport of chemical species. O_3 is particularly suitable as a tracer of atmosphere–surface exchanges because O_3 fluxes are mostly directed downward toward the Earth's surface, acting as an effective O_3 sink (Fig. 14). In fact, O_3 concentration is zero on ground surfaces, as O_3 is consumed on them by thermal decomposition (Turner et al. 1974) or promptly scavenged by reactions with organic compounds, when it dissolves in the water films of vegetation's substomatal cavities (Laisk et al. 1989). These characteristics facilitate data interpretation and understanding of turbulent transport processes that govern the vertical exchange of matter, and provide valuable information on atmospheric and surface resistances for model development. During the DECIPHER campaign, O_3 fluxes were measured above the Alpine grassland near A_1 by means of an eddy-covariance system, which combined a fast-response chemiluminescence O_3 analyzer (COFA, Italy) with a sonic anemometer. The hourly averaged O_3 concentrations and flux observations at site B are reported in Fig. 14. The plot shows that ozone destruction is enhanced during daytime due to the aforementioned O_3 sink given by vegetation. These measurements were complemented by O_3 concentrations recorded at the nearby summit site, enabling the investigation of O_3 transport and deposition in relation to the thermally driven wind system. Finally, tropospheric O_3 is one of the most harmful air pollutants for vegetation (Emberson 2020). Since mountains often experience elevated O_3 concentrations, due to intense solar radiation combined with the transport of precursors from valley bottoms and plains (Finco et al. 2017), measurements of O_3 fluxes allow assessment of the amount of O_3 taken up by grass and the O_3 risk for Alpine vegetation.

---

5. Summary and Outlook

The field campaign performed under the project DECIPHER from June to October 2025 collected a series of coordinated multi-instrument observations of slope-wind development and its coupling with other components of mountain circulations. The measurements also targeted trans-

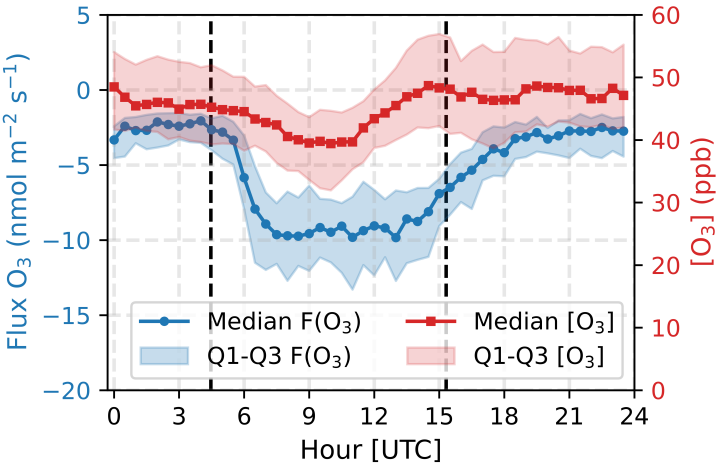


FIG. 14. Ozone fluxes and ozone concentrations at site B. Median daily course of O_3 concentrations (red, right axis) and O_3 fluxes (blue, left axis), with shades representing 25th (Q1) and 75th (Q3) percentiles in the period 21 July - 8 October. The vertical dashed lines represent the average sunrise and sunset times in the study period.

port processes, providing insight into the multi-scale interactions governing the evolution of the MoBL.

Conducted within the TEAMx collaboration, DECIPHER was the only observational campaign located in the southern pre-Alpine range. The preliminary results presented here highlight the variety of processes resolved by the observational setup. These include: ozone exchange at the surface; soil-atmospheric surface properties and exchanges; vertical thermal-dynamic structure and evolution of slope winds through coordinated temperature and wind measurements spanning scales from millimeters near the surface to hundreds of meters above ground, benefiting from sample rates up to more than 1000 Hz; the multi-scale transport of aerosols associated with thermally driven valley and slope circulations. Altogether, these analyses showcase the dataset's potential to investigate connections among near-surface exchanges, slope-flow development, and transport processes.

A major strength of DECIPHER is the combination of complementary measurements across complex Alpine terrain. By resolving processes over a wide range of spatial and temporal scales, the dataset provides a basis for examining exchange within the MoBL and between the slope wind layer, the valley atmosphere, and the overlying free atmosphere. It can therefore support future process-oriented studies, including the evaluation of conceptual models of thermally driven

flows and circulations, the validation of numerical simulations in complex terrain at different spatial scales and resolutions, and the benchmarking of and integration with satellite observations. Building on these potentials, the dataset will also support synergy with other ongoing initiatives and favor the initiation of new ones. In particular, DECIPHER observations are already being used within the Space It Up (`https://spaceitup.it/`) project to complement satellite-based retrievals of the MoBL and to provide a benchmark for drought-related indices. To facilitate broader use, the observations have been made publicly available through an open-access repository on Zenodo (`https://zenodo.org/communities/baldo_monte/`).

Ongoing and planned studies will extend the analyses presented here. These include: the investigation of biological INPs, whose concentrations active at $-11\,^{\circ}\mathrm{C}$ showed stronger day-to-day than within-day variability, with preliminary evidence suggesting a possible influence of rainfall and other environmental conditions over source regions extending hundreds of kilometers upwind; the retrieval of the MoBL and the slope-layer height using DWL carrier-to-noise ratio, in comparison with traditional methods based on the backscattering coefficient; the characterization of the turbulent characteristics in the slope-wind layer and above for turbulence budget investigation; the combination of wind lidar measurements in virtual tower mode and evaluation of the slope-flow 3D variability; the integration of along-slope passive transport of particulate matter. Further work is also addressing the calibration and transferability of low-cost PM sensors in remote and complex terrain, as well as estimating turbulent heat fluxes through the coordinated use of DWL and Raman lidar observations.

Finally, the campaign highlighted practical limitations associated with multi-instrument observations in mountainous environments. Slope-wind conditions occurred during approximately 20% of the observed hours only, due to persistently unfavorable conditions during the campaign. Data availability was further reduced by technical issues and constraints, including low signal-to-noise ratios in DWL measurements under the low-aerosol conditions typical of the clean-air Alpine environment. Therefore, DECIPHER also provided a valuable test of observational strategies and limitations for complex terrain in Italy. The experience gained emphasizes the importance of instrument redundancy, measurement strategies suited to low-aerosol environments, and robust logistical and technical support. These lessons can inform future field campaigns targeting

mountain-atmosphere processes, including initiatives such as TIM (Thunderstorm Intensification from Mountains to Plains Miglietta et al. 2026; Fischer et al. 2025).

Overall, DECIPHER provides an openly available, multi-instrument dataset for investigating surface exchange, slope-wind dynamics, and thermally driven transport across scales. Moreover, it offers a basis for future observational and modeling studies aimed at improving our understanding of transport, exchange, and boundary-layer evolution in complex terrain.

Acknowledgments. The measurement campaign would not have been possible without the continuous assistance from the Civil Protections of Verona and Trento, the townships of Caprino Veronese and Ferrara di Monte Baldo, the city of Mantua Firefighters and the the technicians of the laboratory of Hydraulics of the University of Trento. We also acknowledge the assistance of Prof. Alfonso Vitti (University of Trento) in providing the instrumentation necessary to survey the observational site, and the help of Dr. Luciano Lago (ARPAV) in retrieving the Valeggio sul Mincio X-Band radar data from ARPAV. The DECIPHER project was funded by the European Union under the Next Generation EU PRIN 2022 Prot. n. 2022NEWP4J (CUP B53D23007350006 - W. Cairns; CUP E53D23004450006 - D. Zardi; CUP J53D23002810006- F. Porcù). A. Einbock and F. Conen acknowledge the funding from the Swiss National Science Foundation, grant no. 200020-212121. The author acknowledge the contribution of the consortium "iNEST" (Interconnected Nord-Est Innovation Ecosystem) funded by the European Union under NextGenerationEU (Mission 4.2, Investment 1.5, project no. ECS 00000043 - D. Zardi) The authors also thank the strategic partnership Space It Up!, which is funded by the Italian Space Agency and the Ministry of University and Research - Contract No. 2024-5-E.0 - CUP No. I53D24000060005. C. Brun acknowledges the French National programme LEFE (Les Enveloppes Fluides et l'Environnement) 2024 and the Labex OSUG@2020 Investissements d'avenir ANR10 LABX56. A. Bracci, L. Di Liberto and F. Pasqualini acknowledge the funding from the project IR0000032 – ITINERIS, Italian Integrated Environmental Research Infrastructures System (D.D. no. 130/2022 – CUP B53C22002150006) funded by the EU (Next Generation EU PNRR Mission 4 "Education and Research", Component 2 "From research to business", Investment 3.1 "Fund for the realisation of an integrated system of research and innovation infrastructures").

Data availability statement. Reanalysis data used in this study were obtained from the Copernicus Climate Change Service (C3S) Climate Data Store, including ERA5-Land hourly data (Copernicus Climate Change Service (C3S) 2019), ERA5 hourly data on single (Copernicus Climate Change Service (C3S) 2023b) and pressure levels (Copernicus Climate Change Service (C3S) 2023a), ERA5 daily statistics on single levels (Copernicus Climate Change Service (C3S) 2024), and ERA5 monthly averaged data on pressure levels (Copernicus Climate Change Service (C3S) 2023c). Air-quality data were obtained from the Copernicus Atmosphere Monitoring Service European air quality reanalyses (Copernicus Atmosphere Monitoring Service (CAMS) 2021).

The observational data collected during the campaign is described and organized in the Zenodo community: https://zenodo.org/communities/baldo_monte/. The access to observational data is moderated by a sharing policy reported in the datasets metadata.

APPENDIX A

Observed conditions: Ozone and particulate matter

a. Aerosol-chemistry overview and comparison with climatology

Figure A1 compares the observed daily mean PM loadings and daily maximum ozone concentrations with their counterparts from CAMS global reanalysis (Inness et al. 2019) for 2025, as well as with the climatology for 2013–2025. Except for June and the period from 5 to 20 August, PM loadings, both from CAMS 2025 and from observations, remained below the climatological average. This could be partially due to enhanced deposition processes, probably driven by frequent rain events. The most prominent aerosol peak, observed during the fair-weather days between 9 and 17 August, was probably the result of combined long-range aerosol transport and local accumulation and will be investigated in future studies.

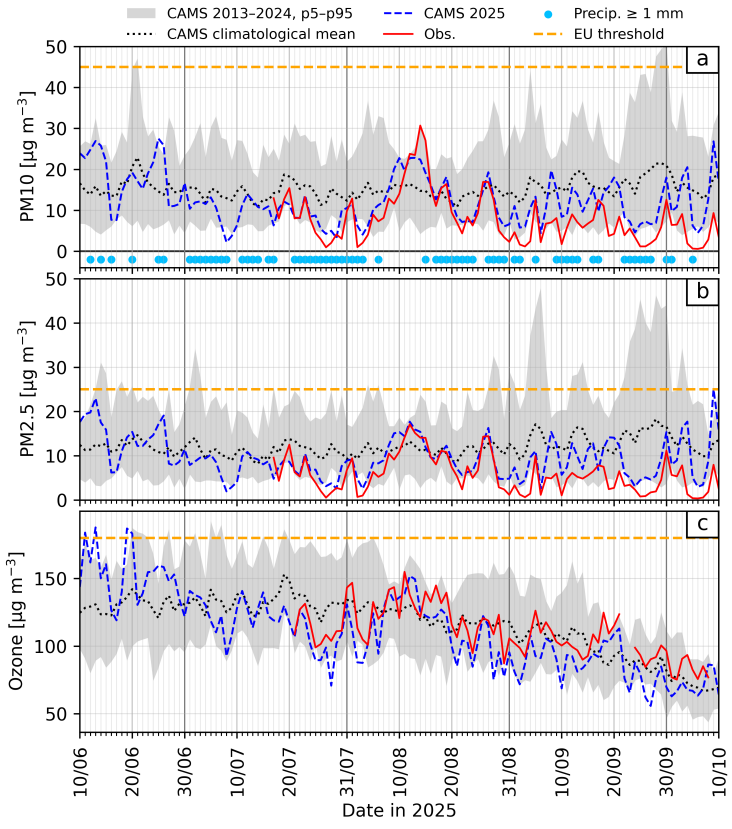
CAMS generally overestimates the observed PM loadings, especially toward autumn. This is probably because the observations shown here are from site C, whereas the corresponding CAMS values (grid spacing of about 10 km) are representative of lower elevations, with a stronger exposure to the Po Plain planetary boundary layer than actually occurs at the site under conditions of limited mixing.

The comparison of daily ozone maxima shows good agreement between the observations and the CAMS results for 2025. The latter are consistently at or below the climatology, except in June and during the fair-weather period in August. This is consistent with the observed meteorological conditions and limited pollutant loading during the campaign.

APPENDIX B

Slope wind conditions

Given that one aim of the campaign is to observe thermally driven slope winds, a multi-factor criterion is assessed to ensure fair-weather conditions conducive to the development of slope winds.



805 FIG. A1. Overview of fine and coarse aerosol counts at A_1. Precipitation is taken from ERA5, PM concentra-
806 tions from the Fidas instrument at C, and ozone concentrations from A_1.

815 Historically, this type of condition has been used to identify slope wind days, i.e., single days
816 conducive to the development of both anabatic and katabatic winds (e.g., Giovannini et al. 2017;
817 Lehner et al. 2019; Farina et al. 2023). However, assessing entire days excludes a large number
818 of anabatic/katabatic regimes, limiting the already few case studies: large-scale and ambient
819 conditions may change throughout the day, shifting from conducive to adverse for thermally driven
820 flows. At the same time, both regimes often favor the temporary development of perturbations that
821 may lead to the exclusion of the entire day, even when only a few hours are affected: this is the case
822 of anabatic winds, where thermals and vertical plumes can detach from the near-surface (Cintolesi
823 et al. 2021), separate from the slope wind and drive the formation of cumulus clouds (Hocut et al.
824 2015), if the ambient stability allows for it. The day within this example would be refused, even
825 though conditions conducive to slope winds may persist over timescales comparable to those of

their forcing. For this reason, we apply the multi-factor criterion to hourly data and mark as "slope wind hours" the blocks of three consecutive hours satisfying it.

The multi-factor criterion consists of a set of ambient (non-local) variables whose values are compared to significant thresholds, in line with the most recent literature. Each condition of the criterion is applied to moving blocks of three hours, with the first considered as a "slope-wind hour" if its block satisfies all the following conditions:

Homogeneity of the high-pressure field This condition aims at excluding synoptic forcing on the local circulation, de facto enabling the development of the local dynamics. It consists of two conditions evaluated on a 2°×2° area around the experimental site as follows:

1. Horizontal gradient of geopotential height Z smaller than $5{\times}10^{-5}$, i.e., half the value for typical mid-latitude cyclones (modified from Lehner et al. 2019): The latitudinal Y and longitudinal X gradients of the geopotential height at 700 hPa are computed (in absolute value) as $\Delta Z/\Delta Y$ and $\Delta Z/\Delta X$, respectively, and averaged to obtain a mean $\langle \Delta Z/\Delta Y \rangle$ and $\langle \Delta Z/\Delta X \rangle$ at each hour. If $\langle \Delta Z/\Delta Y \rangle$ and $\langle \Delta Z/\Delta X \rangle$ are less than 5×10^{-5} for three consecutive hours, this condition is satisfied.
2. High pressure at the surface compared to the 1996-2025 climatological monthly average (modified from Giovannini et al. 2017; Farina et al. 2023): When the daily-average value of the surface pressure is larger than the climatological monthly average, the condition is satisfied for the whole day.

Clear sky This condition aims to exclude the presence of precipitation, clouds, and optically thick atmospheric layers during both day and night, thereby altering the prescribed cycle of the radiation budget. This includes:

1. Clear sky condition using a threshold based on the Clear Sky Index, CSI = $\epsilon_{meas}/\epsilon_{clear-sky}$ (Marty and Philipona 2000). The $\epsilon_{meas} = L_{\downarrow}/\sigma T^4$ ($L_{\downarrow}$ is the downward longwave radiation, $\sigma = 5.67 \times 10^{-8}$ Wm^{-2}K^{-4} is the Stefan-Boltzmann constant and T is the observed air temperature) refers to the emissivity measured at the experimental site; $\epsilon_{clear-sky}$ is the estimated emissivity of clear sky formulated by Prata (1996), that is $\epsilon_{clear-sky} = 1.07\left(1 - \left(1 + 46.5\frac{e}{T}\right) \mathrm{e}^{-\left(1.2+139.5\frac{e}{T}\right)^{1/2}}\right)$, where e is the partial pressure of water vapour in hPa. The condition is satisfied when CSI ≤ 1.

2. Absence of precipitation (Román-Cascón et al. 2019): When the local value of the hourly cumulative precipitation P is smaller than 0.5 mm h^{-1}, the interval is considered non-precipitative, and the condition is satisfied.

3. Maximum solar radiation for the season (modified from Giovannini et al. 2017): The local daily maximum solar radiation is compared with the maximum clear-sky global solar radiation at the surface from ERA5 (Hersbach et al. 2023d). If the local maximum is greater than or equal to the clear-sky radiation, the condition is satisfied.

Weak synoptic forcing This condition requires weak winds approaching the atmospheric boundary layer to exclude atmospheric jets, currents, and fronts that would superimpose on the local wind system.

1. Weak wind speed above the boundary layer (modified from Román-Cascón et al. 2019): when the wind speed at 700 hPa is smaller than 7 m s^{-1}, the condition is satisfied.

For this assessment, gridded data of the ambient variables are collected from ERA5 (Hersbach et al. 2023a,b,c,d), while local data are taken from the experimental site. A critical assessment of this multi-factor criterion and integration with other mountain-terrain datasets will be provided in Carpentari et al., *in preparation*.

References

Banta, R. M., and Coauthors, 2016: *Atmospheric processes over complex terrain*, Meteorological Monographs, Vol. 23. 1st ed., American Meteorological Society, Boston, MA.

Barbano, F., L. Brogno, F. Tampieri, and S. Di Sabatino, 2022: Interaction between waves and turbulence within the nocturnal boundary layer. *Boundary-Layer Meteorology*, **183 (1)**, 35–65.

Bonin, T. A., and Coauthors, 2017: Evaluation of turbulence measurement techniques from a single doppler lidar. *Atmospheric Measurement Techniques*, **10 (8)**, 3021–3039.

Brogno, L., F. Barbano, L. S. Leo, H. J. Fernando, and S. Di Sabatino, 2021: Driving mechanisms of double-nosed low-level jets during materhorn experiment. *Journal of the Atmospheric Sciences*, **78 (12)**, 4037–4051.

Brun, C., S. Blein, and J.-P. Chollet, 2017: Large-eddy simulation of a katabatic jet along a convexly curved slope. part i: Statistical results. *Journal of the Atmospheric Sciences*, **74 (12)**, 4047–4073, https://doi.org/10.1175/JAS-D-16-0152.1.

Charrondiere, C., C. Brun, J.-E. Sicart, J.-M. Cohard, R. Biron, and S. Blein, 2020: Buoyancy effects in the turbulence kinetic energy budget and reynolds stress budget for a katabatic jet over a steep alpine slope. *Boundary-Layer Meteorology*, **177 (1)**, 97–122, https://doi.org/10.1007/s10546-020-00549-2.

Charrondière, C., C. Brun, E. J. Hopfinger, J.-M. Cohard, and J.-E. Sicart, 2022a: Mean flow structure of katabatic winds and turbulent mixing properties. *Journal of Fluid Mechanics*, **941**, A11, https://doi.org/10.1017/jfm.2022.281.

Charrondière, C., and Coauthors, 2022b: Katabatic winds over steep slopes: Overview of a field experiment designed to investigate slope-normal velocity and near-surface turbulence. *Boundary-Layer Meteorology*, **2022**, https://doi.org/10.1007/s10546-021-00644-y.

Chow, F., C. Schär, N. Ban, K. Lundquist, L. Schlemmer, and X. Shi, 2019: Crossing multiple gray zones in the transition from mesoscale to microscale simulation over complex terrain. *Atmosphere (Basel)*, **10 (5)**, 274.

Cintolesi, C., D. Di Santo, F. Barbano, and S. Di Sabatino, 2021: Anabatic flow along a uniformly heated slope studied through large-eddy simulation. *Atmosphere*, **12 (7)**, 850.

Copernicus Atmosphere Monitoring Service (CAMS), 2021: CAMS European air quality reanalyses. Copernicus Atmosphere Monitoring Service Atmosphere Data Store, accessed 1 June 2026, https://doi.org/10.24381/7cc0465a.

Copernicus Climate Change Service (C3S), 2019: ERA5-Land hourly data from 1950 to present. Copernicus Climate Change Service Climate Data Store (CDS), accessed 1 June 2026, https://doi.org/10.24381/cds.e2161bac.

Copernicus Climate Change Service (C3S), 2023a: ERA5 hourly data on pressure levels from 1940 to present. Copernicus Climate Change Service Climate Data Store (CDS), accessed 1 June 2026, https://doi.org/10.24381/cds.bd0915c6.

Copernicus Climate Change Service (C3S), 2023b: ERA5 hourly data on single levels from 1940 to present. Copernicus Climate Change Service Climate Data Store (CDS), accessed 1 June 2026, https://doi.org/10.24381/cds.adbb2d47.

Copernicus Climate Change Service (C3S), 2023c: ERA5 monthly averaged data on pressure levels from 1940 to present. Copernicus Climate Change Service Climate Data Store (CDS), accessed 1 June 2026, https://doi.org/10.24381/cds.6860a573.

Copernicus Climate Change Service (C3S), 2024: ERA5 post-processed daily statistics on single levels from 1940 to present. Copernicus Climate Change Service Climate Data Store (CDS), accessed 1 June 2026, https://doi.org/10.24381/cds.4991cf48.

De Wekker, S. F. J., and M. Kossmann, 2015: Convective boundary layer heights over mountainous terrain—a review of concepts. *Front. Earth Sci.*, **3**, 165 843.

De Wekker, S. F. J., M. Kossmann, J. C. Knievel, L. Giovannini, E. D. Gutmann, and D. Zardi, 2018: Meteorological applications benefiting from an improved understanding of atmospheric exchange processes over mountains. *Atmosphere (Basel)*, **9 (10)**, 371.

Defant, F., 1949: Zur theorie der hangwinde, nebst bemerkungen zur theorie der berg- und talwinde. *Archiv für Meteorologie, Geophysik und Bioklimatologie, Serie A*, **1 (3–4)**, 421–450.

Demko, J. C., and B. Geerts, 2010: A numerical study of the evolving convective boundary layer and orographic circulation around the santa catalina mountains in arizona. part I: Circulation without deep convection. *Mon. Weather Rev.*, **138 (5)**, 1902–1922.

Di Girolamo, P., and Coauthors, 2023: A compact raman lidar for atmospheric CO2 and thermodynamic profiling: The system CONCERNING. *Proceedings of the 30th International Laser Radar Conference*, Springer International Publishing, Cham, 531–537.

Di Paolantonio, M., D. Dionisi, D. Summa, G. Liberti, and P. DiGirolamo, 2026: Raman lidar measurements of CO2 mixing ratio profiles in the lower troposphere: Improved performance capabilities based on state-of-the-art technological solutions and an innovative calibration approach. *Opt. Express*.

Emberson, L., 2020: Effects of ozone on agriculture, forests and grasslands. *Philos. Trans. A Math. Phys. Eng. Sci.*, **378 (2183)**, 20190 327.

Emeis, S., N. Kalthoff, B. Adler, E. Pardyjak, A. Paci, and W. Junkermann, 2018: High-resolution observations of transport and exchange processes in mountainous terrain. *Atmosphere (Basel)*, **9 (12)**, 457.

Farina, S., M. Marchio, F. Barbano, S. di Sabatino, and D. Zardi, 2023: Characterization of the morning transition over the gentle slope of a semi-isolated massif. *J. Appl. Meteorol. Climatol.*, **62 (4)**, 449–466.

Farina, S., and D. Zardi, 2023: Understanding thermally driven slope winds: Recent advances and open questions. *Boundary Layer Meteorol.*, **189 (1-3)**, 5–52.

Fernando, H. J. S., and Coauthors, 2015: The MATERHORN: Unraveling the intricacies of mountain weather. *Bull. Am. Meteorol. Soc.*, **96 (11)**, 1945–1967.

Finco, A., R. Marzuoli, M. Chiesa, and G. Gerosa, 2017: Ozone risk assessment for an alpine larch forest in two vegetative seasons with different approaches: comparison of POD1 and AOT40. *Environ. Sci. Pollut. Res. Int.*, **24 (34)**, 26 238–26 248.

Fischer, J., and Coauthors, 2025: Invited perspectives: Thunderstorm intensification from mountains to plains. *Nat. Hazards Earth Syst. Sci.*, **25 (8)**, 2629–2656.

Geerts, B., Q. Miao, and J. C. Demko, 2008: Pressure perturbations and upslope flow over a heated, isolated mountain. *Mon. Weather Rev.*, **136 (11)**, 4272–4288.

Gianessi, S., and Coauthors, 2024: Testing a novel sensor design to jointly measure cosmic-ray neutrons, muons and gamma rays for non-invasive soil moisture estimation. *Geosci. Instrum. Methods Data Syst.*, **13 (1)**, 9–25.

Giometto, M. G., G. G. Katul, J. Fang, and M. B. Parlange, 2017: Direct numerical simulation of turbulent slope flows up to grashof number. *J. Fluid Mech.*, **829**, 589–620.

Giovannini, L., E. Ferrero, T. Karl, M. W. Rotach, C. Staquet, S. Trini Castelli, and D. Zardi, 2020: Atmospheric pollutant dispersion over complex terrain: Challenges and needs for improving air quality measurements and modeling. *Atmosphere (Basel)*, **11 (6)**, 646.

Giovannini, L., L. Laiti, S. Serafin, and D. Zardi, 2017: The thermally driven diurnal wind system of the adige valley in the italian alps. *Quarterly Journal of the Royal Meteorological Society*, **143 (707)**, 2389–2402.

Giovannini, L., L. Laiti, D. Zardi, and M. de Franceschi, 2015: Climatological characteristics of the ora del garda wind in the alps: Climatological characteristics of the ora del garda wind in the alps. *Int. J. Climatol.*, **35 (14)**, 4103–4115.

Hacker, J., C. Draper, and L. Madaus, 2018: Challenges and opportunities for data assimilation in mountainous environments. *Atmosphere (Basel)*, **9 (4)**, 127.

Hersbach, H., and Coauthors, 2023a: Era5 hourly data on pressure levels from 1940 to present. https://doi.org/https://doi.org/10.24381/cds.bd0915c6.

Hersbach, H., and Coauthors, 2023b: Era5 hourly data on single levels from 1940 to present. https://doi.org/https://doi.org/10.24381/cds.adbb2d47.

Hersbach, H., and Coauthors, 2023c: Era5 monthly averaged data on pressure levels from 1940 to present. https://doi.org/https://doi.org/10.24381/cds.6860a573.

Hersbach, H., and Coauthors, 2023d: Era5 post-processed daily-statistics on single levels from 1940 to present. https://doi.org/https://doi.org/10.24381/cds.4991cf48.

Hocut, C. M., D. Liberzon, and H. J. S. Fernando, 2015: Separation of upslope flow over a uniform slope. *J. Fluid Mech.*, **775**, 266–287.

Inness, A., and Coauthors, 2019: The cams reanalysis of atmospheric composition. *Atmos. Chem. Phys.*, **19**, 3515—3556, https://doi.org/https://doi.org/10.5194/acp-19-3515-2019.

Kirshbaum, D., B. Adler, N. Kalthoff, C. Barthlott, and S. Serafin, 2018: Moist orographic convection: Physical mechanisms and links to surface-exchange processes. *Atmosphere (Basel)*, **9 (3)**, 80.

Laisk, A., O. Kull, and H. Moldau, 1989: Ozone concentration in leaf intercellular air spaces is close to zero. *Plant Physiol.*, **90 (3)**, 1163–1167.

Laiti, L., D. Zardi, M. de Franceschi, G. Rampanelli, and L. Giovannini, 2014: Analysis of the diurnal development of a lake-valley circulation in the alps based on airborne and surface measurements. *Atmos. Chem. Phys.*, **14 (18)**, 9771–9786.

Lehner, M., and M. W. Rotach, 2018: Current challenges in understanding and predicting transport and exchange in the atmosphere over mountainous terrain. *Atmosphere (Basel)*, **9 (7)**, 276.

Lehner, M., M. W. Rotach, and F. Obleitner, 2019: A method to identify synoptically undisturbed, clear-sky conditions for valley-wind analysis. *Boundary-Layer Meteorology*, **173 (3)**, 435–450.

Lehner, M., R. Rotunno, and C. D. Whiteman, 2016: Flow regimes over a basin induced by upstream katabatic flows—an idealized modeling study. *J. Atmos. Sci.*, **73 (10)**, 3821–3842.

Lehner, M., C. D. Whiteman, S. W. Hoch, D. Jensen, E. R. Pardyjak, L. S. Leo, S. Di Sabatino, and H. J. S. Fernando, 2015: A case study of the nocturnal boundary layer evolution on a slope at the foot of a desert mountain. *J. Appl. Meteorol. Climatol.*, **54 (4)**, 732–751.

Lehner, M., and Coauthors, 2026: The TEAMx observational campaign. *arXiv [physics.ao-ph]*.

Leukauf, D., A. Gohm, and M. W. Rotach, 2016: Quantifying horizontal and vertical tracer mass fluxes in an idealized valley during daytime. *Atmos. Chem. Phys.*, **16 (20)**, 13 049–13 066.

Marty, C., and R. Philipona, 2000: The clear-sky index to separate clear-sky from cloudy-sky situations in climate research. *Geophysical Research Letters*, **27 (17)**, 2649–2652.

Menke, R., N. Vasiljević, J. Wagner, S. P. Oncley, and J. Mann, 2020: Multi-lidar wind resource mapping in complex terrain. *Wind Energy Science*, **5 (3)**, 1059–1073.

Miglietta, M. M., and Coauthors, 2026: Severe convective weather in italy: Current understanding and research priorities in the TIM campaign. *Nat. Hazards Earth Syst. Sci.*, **26 (7)**, 3395–3415.

Muñoz Sabater, J., 2019: Era5-land hourly data from 1950 to present. https://doi.org/https://doi.org/10.24381/cds.e2161bac.

Nadeau, D. F., H. J. Oldroyd, E. R. Pardyjak, N. Sommer, S. W. Hoch, and M. B. Parlange, 2020: Field observations of the morning transition over a steep slope in a narrow alpine valley. *Environ. Fluid Mech. (Dordr.)*, **20 (5)**, 1199–1220.

Nadeau, D. F., E. R. Pardyjak, C. W. Higgins, H. Huwald, and M. B. Parlange, 2013: Flow during the evening transition over steep alpine slopes: Evening transition flows over steep alpine slopes. *Q. J. R. Meteorol. Soc.*, **139 (672)**, 607–624.

Obligado, M., Brun C., J. Silvestrini, and B. Camano, 2022: Dissipation scalings in the turbulent boundary layer at moderate re_θ. *Flow Turbulence Combustion*, **108**, 105–122.

Oldroyd, H. J., E. R. Pardyjak, C. W. Higgins, and M. B. Parlange, 2016: Buoyant turbulent kinetic energy production in steep-slope katabatic flow. *Boundary-Layer Meteorology*, **161 (3)**, 405–416.

Pardyjak, E. R., H. Fernando, J. C. R. G. Joseph S. Hunt, and J. Anderson, 2009: A case study of the development of nocturnal slope flows in a wide open valley and associated air quality implications. *Meteorol. Z.*, **18 (1)**, 85–100.

Prandtl, L., 1942: *Führer durch die Strömungslehre*. Friedrich Vieweg & Sohn, Braunschweig, chapter 5, pp. 326–330.

Prata, A., 1996: A new long-wave formula for estimating downward clear-sky radiation at the surface. *Quarterly Journal of the Royal Meteorological Society*, **122 (533)**, 1127–1151.

Rajput, A., and Coauthors, 2026: Disentangling atmospheric transport and mixing processes over mountains: Overview of the preliminary field campaigns of the project DECIPHER, manuscript under review.

Román-Cascón, C., and Coauthors, 2019: Comparing mountain breezes and their impacts on co2 mixing ratios at three contrasting areas. *Atmospheric Research*, **221**, 111–126.

Rotach, M. W., and Coauthors, 2004: Turbulence structure and exchange processes in an alpine valley: The riviera project. *Bull. Am. Meteorol. Soc.*, **85 (9)**, 1367–1386.

Rotach, M. W., and Coauthors, 2022: A collaborative effort to better understand, measure, and model atmospheric exchange processes over mountains. *Bull. Am. Meteorol. Soc.*, **103 (5)**, E1282–E1295.

Serafin, S., and D. Zardi, 2010: Daytime heat transfer processes related to slope flows and turbulent convection in an idealized mountain valley. *J. Atmos. Sci.*, **67 (11)**, 3739–3756.

Serafin, S., and Coauthors, 2018: Exchange processes in the atmospheric boundary layer over mountainous terrain. *Atmosphere (Basel)*, **9 (3)**, 102.

Serafin, S., and Coauthors, 2020: *Multi-scale transport and exchange processes in the atmosphere over mountains*. innsbruck university press, Innsbruck.

Tarquini, S., I. Isola, M. Favalli, A. Battistini, and G. Dotta, 2023: TINITALY: A digital elevation model of italy with a 10-meter cell size. Istituto Nazionale di Geofisica e Vulcanologia (INGV), URL https://doi.org/10.13127/tinitaly/1.1, https://doi.org/10.13127/tinitaly/1.1.

Tarquini, S., I. Isola, M. Favalli, F. Mazzarini, M. Bisson, M. T. Pareschi, and E. Boschi, 2007: TINITALY/01: a new triangular irregular network of italy. *Ann. Geophys.*, **50 (3)**, 407–425.

Turner, N. C., P. E. Waggoner, and S. Rich, 1974: Removal of ozone from the atmosphere by soil and vegetation. *Nature*, **250 (5466)**, 486–489.

Vickers, D., and L. Mahrt, 1997: Quality control and flux sampling problems for tower and aircraft data. *Journal of atmospheric and oceanic technology*, **14 (3)**, 512–526.

Whiteman, C. D., 2000: *Mountain Meteorology: Fundamentals and Applications*. Oxford University Press, Oxford.

Whiteman, C. D., and Coauthors, 2008: Metcrax 2006: Meteorological experiments in arizona's meteor crater. *Bull. Am. Meteorol. Soc.*, **89 (11)**, 1665–1680.

Zardi, D., and S. Serafin, 2015: An analytic solution for time-periodic thermally driven slope flows. *Q. J. R. Meteorol. Soc.*, **141 (690)**, 1968–1974.

Zardi, D., and C. D. Whiteman, 2013: Diurnal mountain wind systems. *Springer Atmospheric Sciences*, Springer Netherlands, Dordrecht, 35–119.

Zreda, M., D. Desilets, T. P. A. Ferré, and R. L. Scott, 2008: Measuring soil moisture content non-invasively at intermediate spatial scale using cosmic-ray neutrons. *Geophys. Res. Lett.*, **35 (21)**.